

The halo of M 49 and its environment as traced by planetary nebulae populations[★]

J. Hartke¹, M. Arnaboldi^{1,2}, A. Longobardi^{3,4}, O. Gerhard⁴, K. C. Freeman⁵, S. Okamura⁶, and F. Nakata⁷

¹ European Southern Observatory, Karl-Schwarzschild-Str. 2, 85748 Garching, Germany
e-mail: [jhartke;marnabol]@eso.org

² INAF, Observatory of Pino Torinese, Turin, Italy

³ Kavli Institute for Astronomy and Astrophysics, Peking University, 5 Yiheyuan Road, Haidian District, Beijing 100871, PR China
e-mail: alongobardi@pku.edu.cn

⁴ Max-Planck-Institut für Extraterrestrische Physik, Giessenbachstrasse, 85748 Garching, Germany
e-mail: gerhard@mpe.mpg.de

⁵ RSAA, Mt. Stromlo Observatory, 2611 Canberra, Australia
e-mail: Kenneth.Freeman@anu.edu.au

⁶ Department of Advanced Sciences, Faculty of Science and Engineering, Hosei University, 184-8584 Tokyo, Japan
e-mail: sadanori.okamura@hosei.ac.jp

⁷ Subaru Telescope, National Astronomical Observatory of Japan, 650 N Aohoku Place Hilo, HI 96720, USA
e-mail: nakata@naoj.org

Received 19 January 2017 / Accepted 10 March 2017

ABSTRACT

Context. The galaxy M 49 (NGC 4472) is the brightest early-type galaxy in the Virgo Cluster. It is located in subcluster B and has an unusually blue, metal-poor outer halo. Planetary nebulae (PNe) are excellent tracers of diffuse galaxy and intragroup light (IGL).

Aims. We aim to present a photometric survey of PNe in the galaxy's extended halo to characterise its PN population, as well as the surrounding IGL of the subcluster B.

Methods. PNe were identified based on their bright [OIII]5007 Å emission and absence of a broad-band continuum through automated detection techniques.

Results. We identify 738 PNe out to a radius of ~155 kpc from M 49's centre from which we define a complete sample of 624 PNe within a limiting magnitude of $m_{5007,lim} = 28.8$. Comparing the PN number density to the broad-band stellar surface brightness profile, we find a variation of the PN-specific frequency (α -parameter) with radius. The outer halo beyond 60 kpc has a 3.2 times higher α -parameter compared to the main galaxy halo ($\alpha_{2.5,inner}^{M49} = (3.20 \pm 0.43) \times 10^{-9} \text{ PN } L_{\odot,bol}^{-1}$), which is likely due to contribution from the surrounding blue IGL. We use the planetary nebulae luminosity function (PNLF) as an indicator of distance and stellar population. Its slope, which correlates empirically with galaxy type, varies within the inner halo. In the eastern quadrant of M 49, the PNLF slope is shallower, indicating an additional localised, bright PN population following an accretion event, likely that of the dwarf irregular galaxy VCC1249. We also determined a distance modulus of $\mu_{PNLF} = 31.29_{-0.08}^{+0.07}$ for M 49, corresponding to a physical distance of 18.1 ± 0.6 Mpc, which agrees with a recent surface-brightness fluctuations distance.

Conclusions. The PN populations in the outer halo of M 49 are consistent with the presence of a main Sérsic galaxy halo with a slight ($B - V$) colour gradient of $10^{-4} \text{ mag arcsec}^{-1}$ surrounded by IGL with a very blue colour of $(B - V) = 0.25$ and a constant surface brightness $\mu_V = 28.0 \text{ mag arcsec}^{-2}$.

Key words. galaxies: individual: M 49 – galaxies: elliptical and lenticular, cD – galaxies: clusters: individual: Virgo – galaxies: halos – planetary nebulae: general

1. Introduction

In the context of hierarchical structure formation, galaxies grow by mergers and accretion of smaller structures (e.g. White & Frenk 1991; Steinmetz & Navarro 2002; Oser et al. 2012) that leave long-lasting signatures in the galaxies' outermost regions, because of long dynamical timescales (of the order of a Gyr at 50 kpc). Early-type galaxies (ETGs) predominantly consist of a very old population of stars that are believed to have formed on a short timescale (~1 Gyr, Thomas et al. 2005, and references therein). The strong size evolution of

massive ETGs, that is, of a factor of between two and four from $z \sim 2$ (e.g. Daddi et al. 2005; van Dokkum et al. 2008) can be explained with a two-phase formation scenario for which the initial phase of violent star formation is followed by accretion events (Oser et al. 2010; Pillepich et al. 2015), whose stellar populations are also old. Hence the distribution of stars and their dynamics at very large radii around massive ETGs should contain important evidence of their accretion histories (Cooper et al. 2013; Cook et al. 2016).

In nearby galaxies, the halos can be mapped with absorption-line spectroscopy of red giant branch (RGB) stars, providing spatial and line-of-sight (LOS) velocity distributions (e.g. McConnachie et al. 2009; Crnojević et al. 2013, 2016). While RGB stars are an excellent tracer to map the halos of the

[★] Based on data collected at Subaru Telescope, which is operated by the National Astronomical Observatory of Japan under programme S14A-006.

Milky Way (MW), M31, or Centaurus A, it becomes too costly to carry out absorption-line spectroscopy for faint sources with apparent magnitudes $m_V > 23.5$ mag.

Integral-field spectroscopy has played a pivotal role in characterising the two-dimensional kinematics of ETGs (Cappellari 2016) within the high surface brightness regions ($1 - 2r_e$). To reach larger distances, discrete tracers are needed to study the halos of bright ETGs. Two common discrete tracers at distances larger than $2r_e$ are planetary nebulae (PNe) and globular clusters (GCs). The latter can be separated into red (metal-rich) and blue (metal-poor) populations, which possess different spatial, velocity, and angular momentum distributions (Coccatto et al. 2013; Pota et al. 2013; Hargis & Rhode 2014). The GC systems in nearby bright ETGs have been studied in multiple surveys (e.g. SLUGGS: Usher et al. 2012; NGVS: Durrell et al. 2014).

PNe are a population of dying asymptotic giant branch (AGB) stars in the zero-age main sequence mass range of $1-8 M_\odot$. The core star strongly emits in the UV. This radiation ionises the envelope of gas surrounding the core star, which re-emits 10% of the UV radiation in one optical line: the [OIII]5007 Å line. It can still be detected in distant galaxies and serves as an identifier of PNe (Dopita et al. 1992). Observational evidence suggests that PNe trace stellar light (e.g. Ciardullo et al. 1989; Coccatto et al. 2009; Cortesi et al. 2013b) and that their angular momentum distribution is that of the stars (e.g. Hui et al. 1995; Arnaboldi et al. 1996, 1998; Méndez et al. 2001). As their luminosity-specific frequency does not vary much with galaxy type (Buzzoni et al. 2006), they are an effective tracer of substructures, which have not been detected in previous imaging or integrated absorption-line spectroscopy, as for example the stellar stream in the M31 disc (Merrett et al. 2006) and the crown in M87 (Longobardi et al. 2015b).

In order to relate the observed properties of the PN population in external galaxies with the properties of the stellar population (e.g. age and metallicity), one characterises the PN population by the luminosity-specific PN number (α -parameter) and the shape of the PN luminosity function (PNLF). Observational evidence suggests that the α -parameter, which relates the stellar luminosity with the number of PN, is further correlated with the integrated ($B - V$) colour of the galaxy (Buzzoni et al. 2006). Ciardullo et al. (1989) analytically describe the shape of the PNLF based on the LF of PNe in M31. The shape of the PNLF is governed by a bright cut-off at m^* . The absolute magnitude M^* of this cut-off is invariant with galaxy type and can therefore be used as a secondary distance indicator to the respective galaxy (Ciardullo et al. 2002).

The Virgo Cluster is an interesting target as there are many indicators for a complex dynamical history. It is one of the closest cluster environments and has already been targeted by a number of PN surveys (Ciardullo et al. 1998; Feldmeier et al. 1998, 2004; Arnaboldi et al. 2002, 2003; Aguerri et al. 2005; Castro-Rodríguez et al. 2009). It is composed of multiple subgroups (Virgo A, B, and C), that were first identified by Binggeli et al. (1987, 1993), centred on the ETGs M87, M49, and M60. The X-ray emission of the hot and dense intergalactic medium is highest at the centres of the subclusters, where the concentration of quiescent galaxies peaks (Schindler et al. 1999). Boselli et al. (2014) observe a colour-segregation effect in the (sub)cluster: red galaxies are located in the high-density regions, whereas blue star-forming galaxies are found in the outskirts of the cluster. Galaxies at the centre of subcluster A are devoid of dusty and gaseous phases of the ISM, while subcluster B mainly consists of star-forming galaxies.

Deep wide-field imaging reveals intricate structures of diffuse intracluster light (ICL) surrounding the bright ETGs, suggesting a hierarchical build-up (Mihos et al. 2005, 2017). This is also reflected in the distribution of intracluster PNe, which show field-to-field variations (Feldmeier et al. 2004; Aguerri et al. 2005; Castro-Rodríguez et al. 2009). The colours of ICL features around the cluster core near the cD galaxy NGC 4486 (M87) are similar to those of M87's halo itself, suggesting that they may have formed from similar progenitors (Rudick et al. 2010).

The galaxy M87 has been the target of a successful pilot survey combining narrow-band photometry from Suprime-Cam at the Subaru telescope (Longobardi et al. 2013, hereafter L13) with high-resolution spectroscopy with FLAMES at the VLT (Longobardi et al. 2015a), uncovering the transition from an inner PN-scarce (old and metal-rich) galaxy to an outer PN-rich, accretion-driven component (young and metal-poor). Longobardi et al. (2015b) identified a recent satellite accretion event through a chevron-like PN structure, that also manifests itself as excess light in the M87 outer halo.

We extended this survey to NGC 4472 (M49), the brightest elliptical galaxy in the Virgo Cluster, residing at the centre of subcluster B. The X-ray bow shock to the north of the galaxy suggests that it is falling into the centre of the Virgo Cluster (Irwin & Sarazin 1996). M49 possesses a system of shells along the major axis, suggestive of past accretion events of satellite galaxies (Janowiecki et al. 2010; Capaccioli et al. 2015). Further substructure is associated with the dwarf galaxy VCC 1249 (UGC 7636). Optical and infrared observations combined with $H\alpha$ measurements show signs of a recent interaction between the dwarf and M49 (Arrigoni Battaia et al. 2012). Côté et al. (2003) mapped the dynamics of M49's GC system within $400''$ (33 kpc), and a more extended photometric GC study mapped M49's halo in its entirety, finding a smooth GC density distribution with radius (Durrell et al. 2014).

This paper is organised as follows: in Sect. 2 we describe the photometric PN survey and the data reduction procedure. The selection and validation of PN candidates is described in Sect. 3. We then study the relation between the azimuthally averaged spatial distribution of the PN candidates and the stellar surface brightness of M49 in Sect. 4. In Sect. 5 we present the PNLF of M49 and the corresponding inferred distance. In Sect. 6 we trace variation of the PNLF in M49's halo with our PN catalogue and discuss whether these are signatures of substructure in Sect. 7. We summarise and conclude in Sect. 8. If not stated otherwise, we assume a distance of 17.1 Mpc (Mei et al. 2007) to M49 that corresponds to a physical scale of 82 pc per $1''$.

2. The Suprime-Cam M49 PN survey

This survey expands the ongoing effort to study PNe as tracers in cluster and group environments. We use the same techniques as L13, who observed M87 at the centre of Virgo's subcluster A using the same instrumental configuration. In order to detect PN candidates, we used a narrow-band filter centred on the [OIII]5007Å-line and measure the colour excess of spatially unresolved sources with respect to the continuum, measured in the broad V -band.

2.1. Imaging and observations

The observations were carried out with the Suprime-Cam at the prime focus of the 8.2 m Subaru telescope (Miyazaki et al. 2002) in May 2014. The $10k \times 8k$ mosaic camera covers an area of

$34' \times 27'$, corresponding to a scale of $0.2''$ per pixel. The halo of M 49 can thus be observed out to a radial distance of 155 kpc with a single pointing.

As we identified PNe using the on-off-band technique (see Sect. 3 for further details), we observe M 49 through a narrow-band [OIII] filter ($\lambda_c = 5029 \text{ \AA}$, $\Delta\lambda = 74 \text{ \AA}$, on-band) and a broad-band V -filter ($\lambda_c = 5500 \text{ \AA}$, $\Delta\lambda = 956 \text{ \AA}$, off-band). The on-band image consists of 13 dithered exposures with a total exposure time of three hours and the off-band image of 14 dithered exposures with a total exposure time of 1.4 h. The exposure time was chosen such that PNe with an apparent narrow-band magnitude of 2.5 mag from the bright cut-off $m_{5007}^* = 26.79$ can still be detected assuming a distance modulus of 30.8 for Virgo. The observations were carried out in one night, with photometric conditions. Throughout the whole night the seeing was better than $0''.7$ and the airmass of the observations varied between 1.1 and 1.5.

2.2. Data reduction, astrometry, and flux calibration

The data were reduced using the instrument pipeline SDFRED¹ for Subaru's Suprime-Cam. As this data set will be used to provide positions of PN candidates for a spectroscopic follow-up, accurate astrometry is needed. We improved the accuracy of the images using the IRAF² package `imcoords` with the 2MASS catalogue as an astrometric reference frame.

In order to flux calibrate the broad-band and narrow-band frames to the AB magnitude system, we observed standard stars through the same filters used for the survey, using the spectrophotometric HILT600 and BD332642 stars for the [OIII]-band and Landolt stars for the V -band. The zero points for the [OIII] and V -band frames normalised to a 1 s exposure are $Z_{[\text{OIII}]} = 24.51 \pm 0.04$ and $Z_V = 27.48 \pm 0.01$. These values are consistent with those obtained by L13, and Castro-Rodríguez et al. (2009), who use the same filters for the Suprime Cam narrow-band photometry.

The integrated flux F_{5007} from the [OIII] line can be related to the magnitude m_{5007} using the following relation (Jacoby 1989)

$$m_{5007} = -2.5 \log_{10} F_{5007} - 13.74, \quad (1)$$

where the flux is in units of $\text{erg cm}^{-2} \text{ s}^{-1}$. Arnaboldi et al. (2003) determine the relation between the AB and m_{5007} magnitudes to be

$$m_{5007} = m_{AB} + 2.49 \quad (2)$$

for the narrow-band filter in use.

The final images are the astrometrically and photometrically calibrated, stacked images in the [OIII] and V -band. We fitted the point spread function (PSF) using the IRAF task `psf`. The best-fit profile is a Gaussian analytical function with a radius $r = 2.36$ pixels and a standard deviation $\sigma = 2.35$ pixels. We also computed the PSF fit in four different image regions separately showing that the PSF does not vary across the image.

¹ <http://www.naoj.org/Observing/Instruments/SCam/sdfred>

² IRAF is distributed by the National Optical Astronomy Observatories, which are operated by the Association of Universities for Research in Astronomy, Inc., under cooperative agreement with the National Science Foundation.

3. Selection of the PN candidates and catalogue extraction

PNe have a bright [OIII]5007 \AA and no continuum emission³. Therefore extragalactic PNe can be identified as objects detected in the on-band [OIII] image, which are not detected in the off-band continuum images, or in other words, which have an excess in [OIII] – V colour. Furthermore PNe are unresolved at extragalactic distances, therefore we only considered point-like objects for analysis. We used the automatic selection procedure developed and validated in Arnaboldi et al. (2002, 2003), subsequently applied to studies of PN populations in Virgo's diffuse ICL (e.g. Castro-Rodríguez et al. 2009) and in Virgo ellipticals. The selection procedure has been tailored to Suprime-Cam data by L13. As the selection procedure is vital to the properties of the extracted catalogue we review the main steps in the following section and refer to Appendix A for further information regarding the basic catalogue extraction.

3.1. Catalogue pre-processing

Throughout the following analysis, we used SExtractor (Bertin & Arnouts 1996) as a tool to detect and carry out photometry of the sources on the images. The narrow- and broad-band magnitudes m_n and m_b are measured in dual-image mode for sources detected on the narrow-band image. In order to determine the limiting magnitude of our survey, we populated the images with a synthetic PN population that follows a Ciardullo-like PNLF and determine the recovery fraction as a function of magnitude. The magnitude at which the recovery fraction drops below 50% is adopted as the limiting magnitude; on the narrow-band image it is $m_{n,\text{lim,cat}} = 26.8$ (AB magnitude) or $m_{5007,\text{lim,cat}} = 29.3$ (see Sect. A.1).

There are different image artefacts that can lead to false detections of PNe. We therefore masked the pixel columns affected by dithering as well as regions with a high background value (e.g. due to charge transfer or saturated stars). Due to the high contribution of diffuse galaxy light we furthermore excluded objects detected within a major-axis radius of $r_{\text{major}} = 159''$ (corresponding to 13 kpc) from the galaxy's centre.

3.2. Object selection

We selected objects as PN candidates based on their position on the colour-magnitude diagram (CMD) and their spatially unresolved light distribution. The CMD selection criteria are shown in Fig. 1. We selected objects with a colour excess of $m_n - m_b \leq -1$ that are brighter than the survey's limiting magnitude $m_{n,\text{lim,cat}} = 26.8$. In order to limit the contamination by foreground stars we then constrained our sample to those objects that fall below the 99.9% confidence limits of a simulated continuum population.

In Figs. 1 and 2 we show the CMD-selected sources that are classified as unresolved or point-like sources. Based on the light distribution of the simulated population, point-sources satisfy the following two criteria: these sources (i) have a half-light radius of $1 < R_h < 3.5$ pixel, where the upper limit corresponds to the 95%-percentile of the simulated population, and (ii) they fall in the region where the difference between m_n and m_{core} is within the 95%-limits of the simulated population (see Appendix A.4).

³ If a faint continuum emission is detected at the position of [OIII] emission, it is likely to be caused by background residuals or crowding.

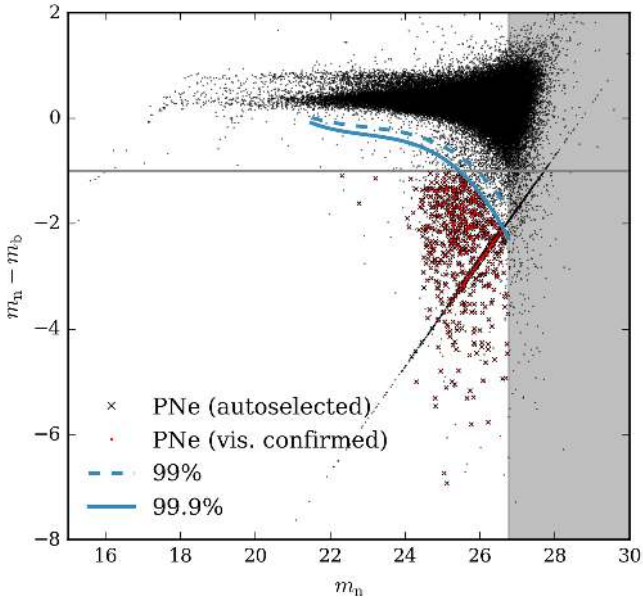


Fig. 1. CMD for all sources in the M 49 Suprime Cam field. Objects below the horizontal line are emission line objects with an $EW_{\text{obs}} > 110 \text{ \AA}$ and colour excess. The solid (dashed) blue lines indicate the regions above which 99.9% (99%) of simulated continuum objects fall. Objects fainter than the limiting magnitude fall into the grey region. The candidate PNe from the automatic selection are denoted by crosses and those confirmed by visual inspection of the images by red dots.

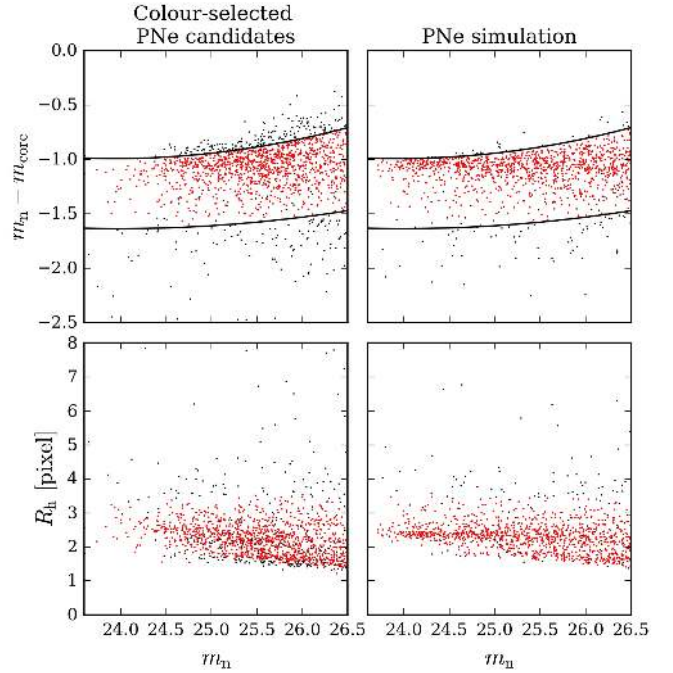


Fig. 2. Point-source test *left column*: colour-selected PNe; *right column*: simulated PN-population. *Top row*: $m_n - m_{\text{core}}$ vs. m_n , the black lines indicate the region in which 95% of the simulated population fall. *Bottom row*: R_h as a function of m_n . We impose a limit of 3.5 pixel on R_h , such that 95% of the simulated population is included. Objects which satisfy both criteria are plotted in red and are termed point-like.

3.3. Catalogue completeness

Evaluating the completeness of our catalogue is a critical step to be carried out before we can use it for further investigation (see Sect. A.5 for further details). We again made use of our synthetic PN population and determined its recovery as a function of radius to assess its spatial completeness ($c_{\text{spatial}}(r)$) and as a function of magnitude for the photometric completeness. For the latter, we independently determined the detection and colour completeness ($c_{\text{detection}}(m_{5007})$ and $c_{\text{colour}}(m_{5007})$ respectively).

3.4. Catalogue validation and visual inspection

The photometric catalogue obtained from the automatic selection was visually inspected and any remaining spurious detections were removed. Spurious detections amounted to $\sim 3\%$ of the automatically extracted sources, the final catalogue contains 735 sources. The visually confirmed PN candidates are shown in Fig. 1. The spatial distribution of the extracted and visually confirmed objects is shown in Fig. 3, superposed on the continuum-subtracted mosaic image.

While the limiting magnitude based on completeness estimations is $m_{5007,\text{lim,cat}} = 29.3$ (see Sect. 3.3), we introduce a more conservative limit of $m_{5007,\text{lim}} = 28.8$ based on the morphology of M 49's PNLf (see Sect. 5). At fainter magnitudes, the PN-number counts decline strongly (Fig. 4). Given that the number of PNe increases exponentially as a function of magnitude beyond the cut-off in old stellar populations (Ciardullo et al. 1989; Longobardi et al. 2015b), such behaviour is indicative of photometric incompleteness. Our final complete sample within $m_{5007,\text{lim}} = 28.8$ consists of 624 PNe.

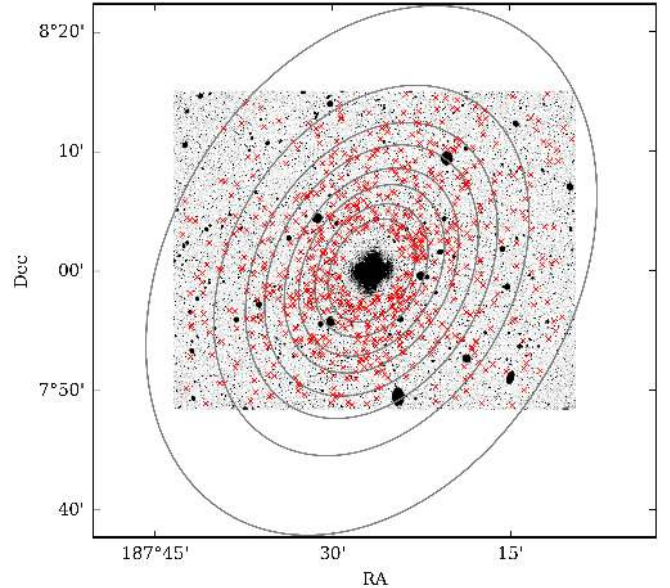


Fig. 3. [OIII] image of M 49 with PN candidates overplotted in red. The elliptical bins have $PA = -31^\circ$ and a constant ellipticity $\epsilon = 0.28$ (K09) and were defined such that they contain the same number of objects. North is up, east is to the left.

3.5. Possible sources of contamination

3.5.1. Contamination by faint continuum objects

As we describe in Sect. A.3, we limited our selection of objects to those that fall below the 99.9%-line of a simulated continuum population in order to minimise the contamination by foreground

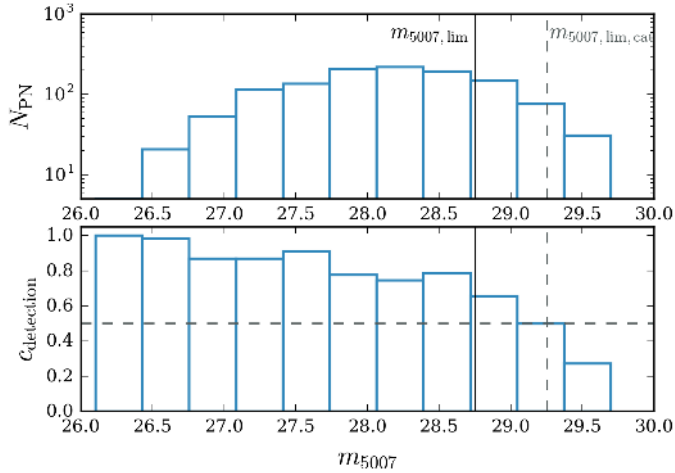


Fig. 4. Observed number counts of PN as function of magnitude (*top panel*) and detection completeness of a simulated PN population (*bottom panel*). The dashed horizontal line denotes the 50% recovery limit that results in the limiting magnitude $m_{5007,\text{lim,cat}} = 29.3$ indicated by the dashed vertical line. The solid vertical line denotes the conservative limiting magnitude $m_{5007,\text{lim}} = 28.8$ based on the decrease of the observed PN-number counts.

objects, for example, faint Milky Way stars. However, some of these objects will be scattered below this line. We estimated the fraction of foreground contaminants in the colour-selected sample by determining the total number of observed foreground stars down to $m_{n,\text{lim}}$ and assuming that 0.1% of these are scattered into the sample of colour-selected PNe. This results in 47 objects, which corresponds to a contribution of 8% of the extracted sample of 624 PNe.

3.5.2. Contamination by background galaxies

Another source of contamination are faint background Ly- α galaxies, that emit at the same wavelength as PNe in the Virgo Cluster, if at redshift $z = 3.1$. In order to quantify this effect, we use the Ly- α luminosity function (LF) determined by Gronwall et al. (2007, hereafter G07), who carried out a deep survey for $z = 3.1$ Ly- α emission-line galaxies. The LF is characterised by a Schechter-function (Schechter 1976). More recent surveys (e.g. Ciardullo et al. 2012) agree with this LF within 0.1 mag. For a detailed description, we refer the reader to L13 who estimated the number of background contaminants for two Suprime-Cam fields covering Virgo’s central galaxy M 87. An important validation of this approach is the confirmation of the number of estimated contaminants during the spectroscopic follow-up of PN candidates (Longobardi et al. 2015a). As our survey is half a magnitude deeper than that of G07, we extrapolate the LF to a limiting magnitude of $m_{5007,\text{lim}} = 28.8$. We expect 310 Ly- α emitters, which corresponds to $(29.8 \pm 6.0)\%$ of the completeness-corrected sample. The corresponding LF is shown in Fig. 10.

Another source of background contaminants are [OII]3727 Å emitters at redshift $z = 0.345$. The colour-selection criterion $m_n - m_b < -1$ corresponds to an observed equivalent width of $EW_{\text{obs}} > 110$ Å, which reduces the contribution from [OII] emitters, as no [OII] emitters beyond $EW_{\text{obs}} > 95$ Å have been observed (Colless et al. 1990; Hammer et al. 1997; Hogg et al. 1998). G07 employ a similar colour-selection criterion ($\Delta m_{\text{G07}} \lesssim -1$) and consider the fraction of [OII] contaminants at redshift $z = 0.345$ negligible. Therefore the contribution of background

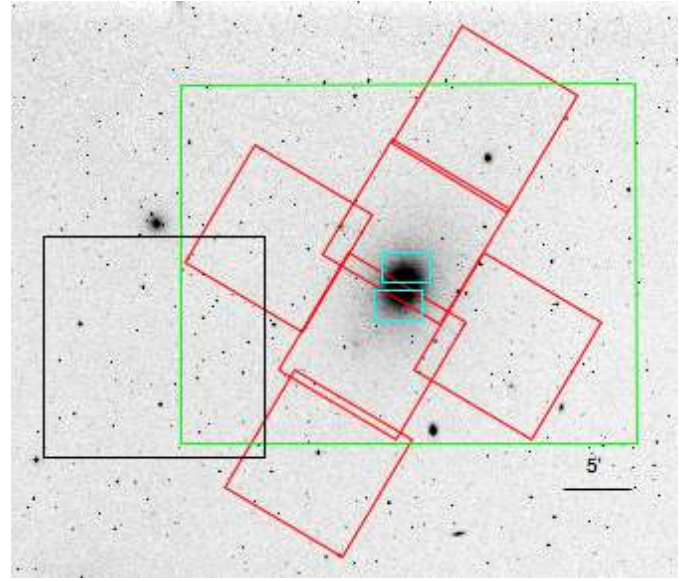


Fig. 5. DSS image of M 49 with PN survey fields overplotted. Green: this survey, cyan: Jacoby et al. (1990), black: Feldmeier et al. (2003), red: PN.S (Pulsoni et al., in prep.).

[OII] emitters with $EW_{\text{obs}} > 110$ Å is accounted for when using the G07 Ly- α LF.

3.6. Comparison with other PN-surveys of M 49

The first survey of PNe in M 49 was carried out by Jacoby et al. (1990). They detected 54 objects with [OIII] excess, of which 27 belong to the statistically complete sample as defined by the authors. This survey consists of two $3'5 \times 2'2$ CFHT fields that cover the central region of M 49 and are indicated in Fig. 5 (cyan rectangles). As the majority of this region is masked out in our deep images, only one common PN candidate is identified. We will discuss the comparison between our PNLF and that of Jacoby et al. (1990) in Sect. 5.

Our survey also overlaps with a previous photometric study of intracluster PNe (Feldmeier et al. 2003, 2004). The field that overlaps with our survey is denoted by a black rectangle in Fig. 5 and has been observed with the Prime Focus CCD camera at the Kitt Peak National Observatory (KPNO) 4 m telescope. The survey depth in the [OIII] is $m_{5007} = 28$ mag. A cross-matching of the survey with our catalogue identifies six common objects. The comparison of the [OIII] magnitudes is shown in Fig. 6. An average zero-point offset of 0.5 mag is found. A previous comparison of M 87’s PN sample from Suprime Cam photometry L13 with PNe identified by Feldmeier et al. (2003) found an offset in magnitude zero-point that equalled to 0.3 mag.

Currently there is no published spectroscopic PNe data for M 49 available. However, we have access to unpublished data from the Planetary Nebula Spectrograph (PN.S, Douglas et al. 2002) as part of a survey of ETGs (Pulsoni et al., in prep.). Of the six PN.S fields ($10' \times 10'$, indicated in red in Fig. 5) four are aligned along the major axis and two along the minor axis, covering $18'$ and $15'$ along the respective axis, extending a little further along the major axis than our survey. In total, 465 PNe have been detected, of which 226 fall into the unmasked regions of our observations. The PN.S is capable of detecting PNe in the Virgo Cluster down to $\Delta m = 1.5$ from the bright cut-off. We therefore matched only PNe in this magnitude range with the PN.S catalogue. There are 207 PNe in common within a matching radius

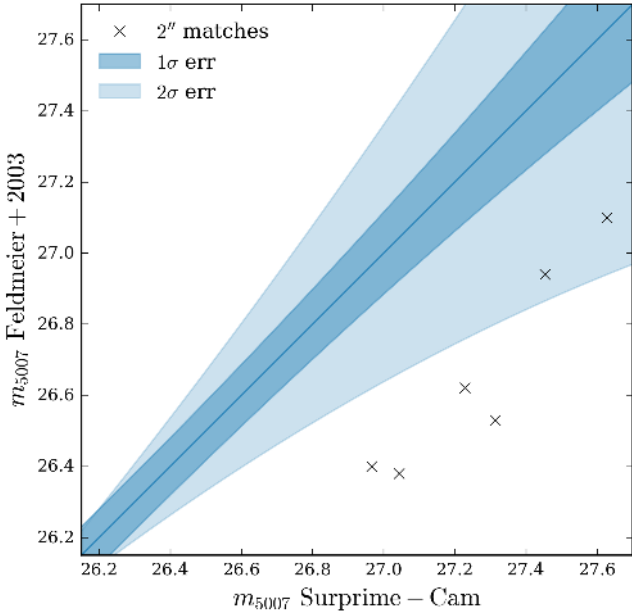


Fig. 6. Magnitude comparison and photometric error of the matched emission-line objects between our catalogue and Feldmeier et al. (2003).

of $5''$, which serves as a first spectroscopic confirmation of these sources.

4. The radial PN number density profile and the PN luminosity-specific frequency

In the following section we determine the radial PN number density profile and compare it to stellar surface brightness profiles derived from broad-band photometric studies of the M 49 halo. Empirically, it has been shown that the PN number density profile follows the stellar light in elliptical (L13; Coccato et al. 2009; Longobardi et al. 2015b) and S0 galaxies (Cortesi et al. 2013a,b). In the last decade, there have been a number of deep photometric surveys of the Virgo cluster. In this section, we will discuss the surface brightness profile and the 2D properties of the stellar light in M 49’s extended halo. In a cluster environment, surface brightness and colour profiles do not only provide important evidence about the galaxy halo, but also about its environment, the ICL. Our goal is to link the structural components in the light, which are signalled by a change of slope in the radial gradients of the SB profile, isophotal twists, and different colour gradients, with variations in the PN population parameters as the number density profile, PNLF slopes and the α -parameter.

4.1. Stellar surface photometry of M 49

The stellar surface brightness profile of ETGs is well-described by a Sérsic function (Sérsic 1963) of the form

$$I(r) = 10^{-0.4\mu_e} 10^{-b((r/r_e)^{1/n}-1)}, \quad (3)$$

with $b = 0.868n_V - 0.142$. For M 49, Kormendy et al. (2009, hereafter K09) determine the major-axis fit parameters in the V-band to be $\mu_{e,V} = 23.371^{+0.171}_{-0.144}$ mag arcsec $^{-2}$, $r_{e,V} = 269.291^{+23.634}_{-18.570}$ arcsec, and $n_V = 5.992^{+0.314}_{-0.292}$. The Sérsic profile is also fit to data from a deep V-band imaging survey of diffuse light in the Virgo Cluster (Janowiecki et al. 2010), the

fit-parameters agreeing within $1 - 2\sigma$ with K09. The effective radius derived from integration of the 2D profile is $r_e = 194.44 \pm 17.0''$.

More extended photometry from the VEGAS survey (Capaccioli et al. 2015, hereafter C15) is also well-fit by a Sérsic profile with an effective radius of $r_e = 152'' \pm 7''$ in both the g - and i -bands⁴. The g -band profile changes slope beyond a major-axis distance of $r \sim 915''$. A hint of this flattening at large radii can also be seen in the i -band and was also already observed in the surface brightness profile derived from photographic plates by Caon et al. (1994). Figure 7 shows the V- and g -band stellar surface brightness profiles of K09 and C15 as well as the Sérsic fit determined by K09.

Beyond a major-axis distance of $r \sim 250''$ the orientation and morphology of the isophotes change. The position angle, which is at constant -20° for the main galaxy halo, rapidly decreases from -20° to -40° in the g - and V-band and rapidly increases from -20° to -5° in the i -band. Furthermore, the isophotal ellipticity ϵ changes: the g - and V-band isophotes become more elongated, reaching a maximum ellipticity of $\epsilon \approx 0.3$, while the i -band isophotes become nearly round ($\epsilon \approx 0$, C15, see Fig. 7 therein).

Gonzalez et al. (2005) suggest that the rapid variation of the isophotes’ parameters as well as the flattening of the surface brightness profile at large radii is likely due to a population of ICL. The flattening of the surface brightness profile occurs at a surface brightness level of $\mu_g \sim 27$ mag arcsec $^{-2}$ (C15), which is compatible with the surface brightness where a ICL-induced change of slope is observed in a sample of stacked SDSS galaxy clusters between redshift $z = 0.2$ and 0.3 (Zibetti et al. 2005). In the case of M 49, which is located at the heart of the Virgo subcluster B, this extra light is probably not intracluster light from the main Virgo Cluster, but rather intragroup light (IGL, Rudick et al. 2006; Gonzalez et al. 2005) of the subcluster B.

The colour profile of M 49 has a clear gradient that is shallow in the red, inner regions and steepens towards the bluer outskirts (Mihos et al. 2013, C15). The transition from shallow to steep gradient occurs at $r \sim 200''$, similar to where the isophotes start to change ellipticity and orientation. There are at least two causes for such a colour gradient, which might be interlinked. It can be interpreted as a metallicity gradient from a metal-rich to a metal-poor component, but also as an age gradient from an older to a younger population. This supports the assumption of a two-component galaxy halo with a change of halo composition in the outer part. When comparing the results of the VEGAS survey (C15) with the ones of Mihos et al. (2013, 2017), the VST broad-band images show an extended outer envelope that is responsible for the change of slope in the surface brightness profile beyond $r^{1/4} = 5.5$. The most reliable measurement of the envelope’s colour is that of Mihos et al. (2013) of $(B - V) = 0.66 \pm 0.02$ at $r^{1/4} = 6.0$.

In the remainder of this section, we wish to investigate whether we observe similar trends in our PN sample. Signatures are expected to be found in the radial PN number density profile and the α -parameters.

4.2. The radial PN number density profile

Figure 3 shows the distribution of PNe on the sky together with elliptical bins, aligned with the photometric major axis with a PA = -31° and a constant ellipticity $\epsilon = 0.28$ as measured from isophotes (K09). The binning has been chosen such that every

⁴ In order to match the g -band photometry to the V-band photometry of K09, we adopted a constant offset of -0.35 as determined by C15.

bin contains the same number of objects (~ 70). The PN logarithmic number density profile is defined as

$$\mu_{\text{PN}}(r) = -2.5 \log_{10} \Sigma_{\text{PN}}(r) + \mu_0, \quad (4)$$

where μ_0 is a constant in order to match the PN number density profile with the stellar surface brightness profile and Σ_{PN} is the completeness-corrected PN number density. As detailed in Sect. 3.3 we have to account for colour and spatial incompleteness (c_{colour} and c_{spatial} respectively) that have been determined in Sect. 3.3 and detailed values are given in Appendix A, Tables A.1 and B.1. The total number of expected PNe is thus

$$N_{\text{PN,corr}}(r) = \frac{N_{\text{PN,obs}}(r)}{c_{\text{spatial}}(r)c_{\text{colour}}}, \quad (5)$$

and the number density is

$$\Sigma_{\text{PN}}(r) = \frac{N_{\text{PN,corr}}(r)}{A(r)}. \quad (6)$$

The area $A(r)$ is the area of intersection of the elliptical annulus with the field of view of the observation, accounting for the regions that have been masked, which was computed using Monte-Carlo integration techniques.

As explained in Sect. 3.5.2, we also need to account for background galaxies at $z = 3.1$ emitting Ly- α radiation redshifted to our narrow-band filter range. We therefore statistically subtracted the contribution of Ly- α emitters from the completeness corrected number of PNe $N_{\text{PN,corr}}$. We assume a homogeneous distribution in the surveyed area, accounting for a 20% variation in the Ly- α LF due to large-scale cosmic variance (cf. Appendix B). We calculated the number density profile adopting a limiting magnitude of $m_{5007,\text{lim}} = 28.8$ (see Sect. 3.4). Given that the PNLF bright cut-off is at $m_{5007}^* = 26.8$ (see Sect. 5), we span a magnitude range of $\Delta m = 2$.

The resulting density profile matched to the V-band surface brightness profile (K09) is shown in Fig. 7. We also computed the number density profile for all PNe down to the automatically determined limiting magnitude $m_{5007,\text{lim}} = 29.3$ and only find a constant offset to the magnitude-limited sample which does not depend on radius. We cover a radial range of $250''$ to $1785''$, corresponding to 20 to 155 kpc, spanning $9r_e^5$. The error bars account for the counting statistics and the uncertainty on the Ly- α LF.

The PN number density profile follows the stellar light closely out to a radius of $r \sim 730''$. At larger radii it starts to flatten and diverges from the Sérsic profile. We note that the flattening occurs much earlier than for the stellar surface brightness profile, but seems to have a steeper slope compared to the flattened part of the stellar profile. As we statistically subtracted the contribution from Ly- α background galaxies, we do not expect the flattening to be due to Ly- α emitters (see also L13, Sect. 4.1). The origin of the flattening of the logarithmic PN number density is investigated in the following.

4.3. The PN luminosity-specific number – the α -parameter

Before we fit a model to the PN number density profile, we need to establish the connection between the PN population and the underlying stellar population. The total number of PNe can be directly related with the total bolometric luminosity L_{bol} of the parent stellar population via the so-called α -parameter:

$$N_{\text{PN}} = \alpha L_{\text{bol}}. \quad (7)$$

⁵ Assuming the effective radius from the 2D profile integration of K09.

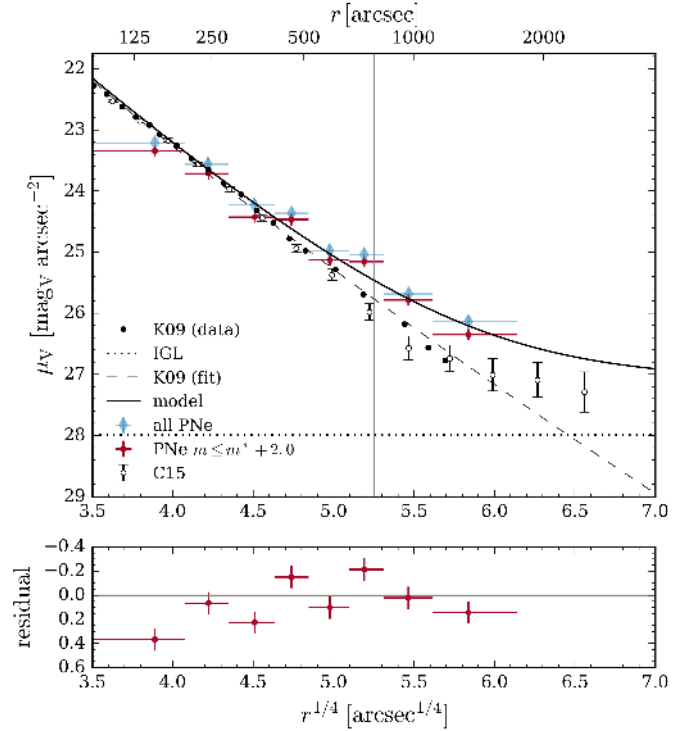


Fig. 7. *Top panel:* radial surface brightness profiles in M49: the filled circles denote the surface brightness profile observed by K09 and the open circles are from C15. The Sérsic fit (K09) is indicated by the dashed line. The dotted horizontal line shows the expected contribution of the IGL. The PN number density profile is denoted with blue diamonds and red circles, where the latter sample has a magnitude limit of $m^* + 2.0$ mag. The two-component model fit to the PN number density profile is shown with the solid black line. The vertical line denotes the transition radius from the inner PN-scarce to the outer PN-rich halo based on the change in the PN number density slope. *Bottom panel:* residuals of the fit.

As our survey is magnitude-limited to $\Delta m = 2$ mag from the bright cut-off, we first determined the α -parameter for that magnitude range, which is defined to be

$$N_{\text{PN},\Delta m} = \int_{m^*}^{m^*+\Delta m} N(m) dm = \alpha_{\Delta m} L_{\text{bol}}, \quad (8)$$

where $N(m)$ is the PNLF and $m_{5007}^* = 26.8$ its apparent bright cut-off magnitude.

If we sample the entire stellar population, we can determine the total number of PNe associated to a parent stellar population with total bolometric luminosity L_{bol} under the assumption that the luminosity-specific stellar death rate is approximately independent of its parent population's age, metallicity, and initial mass function (Renzini & Buzzoni 1986):

$$N_{\text{PN}} = B L_{\text{bol}} \tau_{\text{PN}}, \quad (9)$$

where τ_{PN} is the PN visibility lifetime and B is the specific evolutionary flux⁶. Combining Eqs. (7) and (9) one can determine the luminosity-specific PN number:

$$\alpha = \frac{N_{\text{PN}}}{L_{\text{bol}}} = B \tau_{\text{PN}}. \quad (10)$$

⁶ The evolutionary flux quantifies the stellar death rate based on the flow of stars through post-main sequence evolutionary stages. Normalising this quantity by the unit light of the stellar population one gets the specific evolutionary flux (see e.g. Greggio & Renzini 2011).

Simulations of simple stellar populations predict that the variations of B with metallicity or Initial Mass Function (IMF) are small – values of B are in the range of $1-2 \times 10^{-11} L_{\odot}^{-1} \text{ yr}^{-1}$ for simulated simple stellar populations (Renzini & Buzzoni 1986) – thus one can understand the observed values of the α -parameter as a proxy for the visibility lifetime τ_{PN} of the PNe associated with the parent stellar populations. For PN-surveys that do not have the sensitivity to span the entire PNLf, the luminosity specific alpha-parameter provides an estimate of the PN visibility lifetime within the limiting magnitude of the survey.

4.4. A two-component photometric model for M49

The flattening of PN number density profile at large radii might be due to an additional outer component. This can be a secondary component of M49's halo, or the diffuse light component of the Virgo subcluster B (IGL), at whose centre M49 resides (Binggeli et al. 1987, 1993). We therefore constructed a two-component photometric model in order to reproduce the flattening at large radii. A change of slope is also observed in the stellar surface brightness profile, but at larger radii (C15).

The inner component is dominated by a Sérsic profile. As the slope of the outer stellar surface brightness profile has not been fitted to date, we followed the suggestion of L13 to use a constant surface brightness for the IGL component. We determined this component's value by determining the differential surface brightness between the last measured value of the flattened stellar profile (C15) and the extrapolated Sérsic fit at that radius and find $\mu_{\text{outer}} = 28.0 \text{ mag arcsec}^{-2}$.

The photometric model for the predicted PN surface density is then

$$\tilde{\Sigma}(r) = (\alpha_{\Delta m, \text{inner}} I_{\text{inner, bol}}(r) + \alpha_{\Delta m, \text{outer}} I_{\text{outer, bol}}(r)) s^2 \quad (11)$$

$$= \alpha_{\Delta m, \text{inner}} \left(I_{\text{inner, bol}}(r) + \left(\frac{\alpha_{\Delta m, \text{outer}}}{\alpha_{\Delta m, \text{inner}}} - 1 \right) I_{\Delta m, \text{outer, bol}}(r) \right) s^2. \quad (12)$$

The two components $I_{\text{inner, bol}}(r)$ and $I_{\text{outer, bol}}(r)$ are the bolometric surface brightness profiles related by the α -parameters of the respective populations and $s = D/206265$ is a scale factor related to the galaxy's distance D . The bolometric correction is done via

$$I = 10^{-0.4(\text{BC}_V - \text{BC}_{\odot})} 10^{-0.4(\mu - K)}, \quad (13)$$

with the solar bolometric correction $\text{BC}_{\odot} = -0.07$, and $K = 26.4 \text{ mag arcsec}^{-2}$ is the V -band conversion factor to physical units $L_{\odot} \text{ pc}^{-2}$. One can assume a fixed value of $\text{BC}_V = -0.85$ with 10% accuracy based on the study of stellar population models for different galaxy types (irregular to elliptical, see Buzzoni et al. 2006).

In order to determine the α -parameter of the inner component, we matched PN surface density (Eq. (4)) to the stellar surface brightness profile in the V -band (K09) in the inner region, where the two profiles follow each other closely. The α -parameter can then be determined from the offset μ_0 between the two profiles and applying the bolometric correction:

$$\alpha_{\text{inner}} = \frac{10^{0.4(\mu_0 - K - (\text{BC}_{\odot} - \text{BC}_V))}}{s^2}. \quad (14)$$

Within the chosen magnitude range ($\Delta m = 2$), we determined an offset of $\mu_0 = 15.0 \pm 0.1 \text{ mag arcsec}^{-2}$, corresponding to $\alpha_{2, \text{inner}} = (1.99 \pm 0.27) \times 10^{-9} \text{ PN } L_{\odot, \text{bol}}^{-1}$.

We then fitted the two-component model to the observed PN number density profile over the whole radial range. As we have already determined $\alpha_{2, \text{inner}}$, the only free parameter is the ratio of the two parameters $\alpha_{\Delta m, \text{outer}}/\alpha_{\Delta m, \text{inner}}$, which is determined using the fit algorithm `lmfit` (Newville et al. 2014). The best-fit ratio is $\alpha_{2, \text{outer}}/\alpha_{2, \text{inner}} = 3.21 \pm 0.54$ with $\chi_{\text{red}}^2 = 2.9$ and the resulting best-fit model is denoted by the black line in Fig. 7.

A common magnitude range in which α -parameters are evaluated is within $\Delta m = 2.5 \text{ mag}$ from the bright cut-off. We can extrapolate $\alpha_{2.5}$ to from a sample that is only complete to a magnitude $m_c < m^* + 2.5$ using the following relation

$$\alpha_{2.5} = \Delta m_c \times \alpha_{m_c} \quad (15)$$

with

$$\Delta m_c = \frac{\int_{m^*}^{m^*+2.5} N(m) dm}{\int_{m^*}^{m_c} N(m) dm}, \quad (16)$$

derived from Eq. (8).

In Sect. 5 we derive the PNLf of M49, which we use here as $N(m)$. For $m_c = m^* + 2 = m_2$, the extrapolation factor to $\alpha_{2.5}$ is $\Delta_2 = 1.6$, which results in the following parameters:

- $\alpha_{2.5, \text{inner}}^{\text{M49}} = (3.20 \pm 0.43) \times 10^{-9} \text{ PN } L_{\odot, \text{bol}}^{-1}$ for the inner component, and
- $\alpha_{2.5, \text{outer}}^{\text{M49}} = (1.03 \pm 0.22) \times 10^{-8} \text{ PN } L_{\odot, \text{bol}}^{-1}$ for the outer component.

For comparison, Jacoby et al. (1990) determine $\alpha_{2.5} = (6.5 \pm 1.4) \times 10^{-9} \text{ PN } L_{\odot, \text{bol}}^{-1}$ for the very inner regions of M49.

We find that the outer halo has an α -parameter that is 3.2 times higher compared to the inner halo. This is suggestive of a change of the parent stellar population with radius. This might be due to a contribution of intragroup PNe from the subcluster B to the outer halo, as was observed for M87 in Virgo's subcluster A (L13; Longobardi et al. 2015a).

Combining the two-component PN number density model with the colour profile from Mihos et al. (2013), we were able to evaluate the relation between α -parameter and $(B - V)$ colour continuously for the entire galaxy. Motivated by the two-component photometric model described earlier in this section, we extended this approach to the colour profile. At each radius the colour was calculated as the luminosity-weighted average from each component, whose spatial distribution is given by the PN surface-density decomposition. We allowed for a radially dependent colour profile in the inner halo that has the form

$$(B - V)_{\text{inner}}(r) = \Delta_i r + (B - V)_i, \quad (17)$$

where the best fit results in a colour gradient of $\Delta_i = (-1.0 \pm 0.4) \times 10^{-4} \text{ mag arcsec}^{-1}$ and $(B - V)_i = (B - V)_{\text{inner}}(r = 0) = 0.96 \pm 0.01$ with a constant outer colour of $(B - V)_{\text{outer}} = 0.25 \pm 0.11$. The resulting total colour profile is in agreement with the new extended photometry of Mihos et al. (2017). The bluer colour of the IGL is in line with younger, more metal-poor IGL components identified in cosmological simulations (Cui et al. 2014).

Figure 8 shows the relation for the modelled α -parameter as a function of galaxy colour computed from the above model compared to data points of individual galaxies from previous PN surveys of early-type and Local Group (LG) galaxies collected by Buzzoni et al. (2006, and references therein). We scale our α -parameters from $\alpha_{2.5}$ to α_8 using Eq. (16) based on the best-fit PNLf (Sect. 5) in order to use the same reference

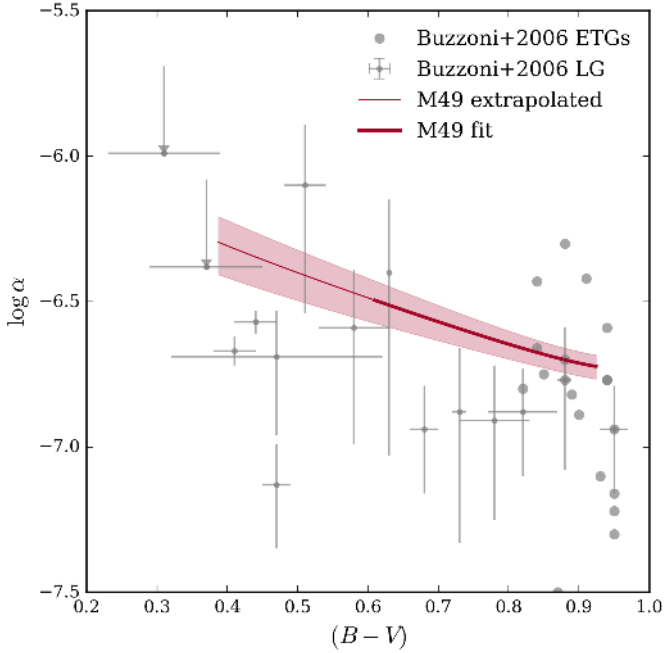


Fig. 8. Variation of the α -parameter in M 49 with colour (red line, colour data from Mihos et al. 2013) compared to data from previous PN surveys in Local Group galaxies (grey error bars) and ETGs (grey circles) based on Buzzoni et al. (2006) and references therein. The result for M 49 is based on the two-component model presented in Sect. 4.4. The thinner line denotes data exceeding the radial range of the colours measured by Mihos et al. (2013) where the colours have been extrapolated based on the model in Sect. 4.4.

system as Buzzoni et al. (2006). As our survey spans a radial range that is $\sim 500''$ larger compared to Mihos et al. (2013), the colour profile has been extrapolated from $1260''$ to $1785''$ based on our best-fit model. The relation between α and $(B - V)$ colour can be approximated with the following second order polynomial:

$$\alpha(B - V) = 0.34(B - V)^2 - 1.25(B - V) - 5.86. \quad (18)$$

The α -parameter is lowest in the inner, red, metal-rich halo, as it would be empirically expected from bright ETGs. It increases with decreasing colour and is highest in the metal-poor, blue, outer halo, similar to the star-forming LG galaxies with this colour.

4.5. Comparison to GCs in M 49's halo

GCs are another tracer of faint extended galaxy halos. The Next Generation Virgo Survey (NGVS, Ferrarese et al. 2012) covers the subclusters A and B out to their virial radii, being sufficiently deep to detect GCs (Durrell et al. 2014). The GC density profiles shown in Fig. 9 are obtained through isophote-fitting of the smoothed red (RGC) and blue (BGC) distributions. In order to compare with the PN number density, we match the distribution of the RGCs to the stellar light in the inner halo (K09). The number density of the PNe and the RGCs agree out to a radius $r^{1/4} = 5.5$, which is where the PNe also start to deviate from the stellar light. The density profile of the BGCs is flatter than both the stellar light and the PN density over the entire radial range covered by both surveys.

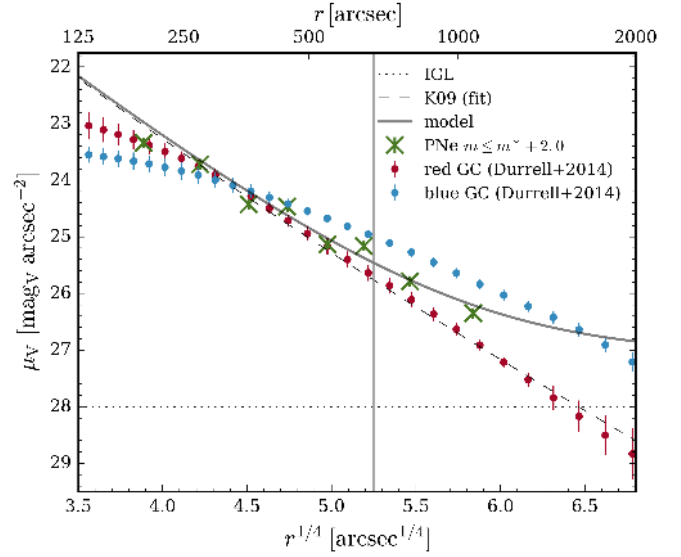


Fig. 9. Comparison of the PN number density profile with that of red and blue globular clusters. The Sérsic fit to broad-band photometry (K09) is indicated by the dashed line. The dotted line shows expected contribution of the IGL. The PN number density profile is shown with green crosses and the two-component model fit to it is denoted with the solid grey line. The density profile from red and blue globular clusters are indicated by filled circles in the respective colours. The vertical line denotes the transition radius from the inner to the outer halo based on the change in the PN number density slope.

5. The planetary nebula luminosity function of M 49

Another characteristic of a PN sample is the shape of its luminosity function (PNLF). As there is empirical evidence for a bright cut-off of the luminosity function, which is consistent with a nearly constant absolute magnitude, the PNLF can be used as a secondary distance indicator (Ciardullo et al. 2002). This cut-off is found to be invariant between different Hubble types (Ciardullo et al. 2004). We compared the PNLF of our completeness-corrected PN sample to the generalised analytical formula introduced by L13

$$N(M) = c_1 e^{c_2 M} (1 - e^{3(M^* - M)}), \quad (19)$$

where c_1 is a normalisation constant, c_2 is the slope at the faint end, and M^* is the absolute magnitude of the LF's bright cut-off. The Ciardullo et al. (1989) analytical LF is then a specific case of Eq. (19) with $c_2 = 0.307$ that reproduces the best fit to the PNLF of M 31. It describes the exponential envelope expansion (Henze & Westerlund 1963) combined with a sharp exponential truncation at the bright end. Observations also suggest that the slope described by the parameter c_2 is correlated with the star formation history of the parent stellar population. Steeper slopes are associated with older stellar populations and conversely flatter slopes with younger populations (L13; Ciardullo et al. 2004; Ciardullo 2010).

The left panel of Fig. 10 shows the PNLF of the data corrected for detection and colour incompleteness before having subtracted the contribution from Ly- α emitting galaxies together with the expected LF of these objects (G07). The panel also shows the PNLF expected for a galaxy at the distance of M 49 (Mei et al. 2007) based on Eq. (19), with $c_2 = 0.307$, normalised to the number of objects in our sample. Furthermore, compared to the bright cut-off of the expected PNLF, there are a number of

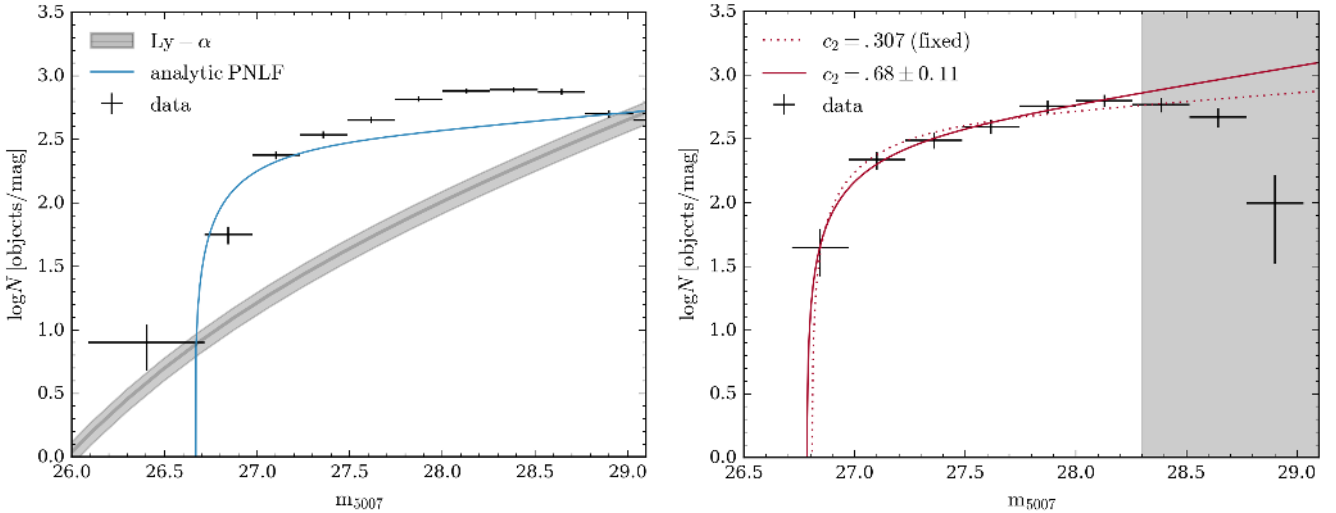


Fig. 10. *Left:* PNLF of the completeness-corrected PN sample (without accounting for contamination by Ly- α -emitting background galaxies). The error bars along the y -axis account for the Poissonian error and the x -errors for the bin width. The solid blue line shows the analytical PNLF at a distance modulus $\mu = 31.3$ with $c_2 = 0.307$ (Ciardullo et al. 1989). The solid grey line shows the Ly- α LF (G07) and its variance due to density fluctuations is represented by the shaded region. *Right:* PNLF of the completeness-corrected PN sample after statistical subtraction of the estimated Ly- α LF. The grey region denotes the magnitude range in which the PNLF might be affected by incompleteness that could not be corrected for. The error bars along the y -axis account for the Poissonian error and the x -errors for the bin width. The solid red line shows the fit of the generalised PNLF, with the best-fit parameters $c_2 = 0.69 \pm 0.12$ and $\mu = 31.29 \pm 0.05$. The dotted line shows the fit to the PNLF for $c_2 = 0.307$ (Ciardullo et al. 1989).

overluminous objects, whose nature we will discuss in the next section.

We calculated the PNLF of our PN catalogue, corrected it for detection and colour incompleteness as a function of magnitude (see Sect. 3.3 for details), and statistically subtracted the expected number of Ly- α emitters in each magnitude bin based on the G07 LF. The right panel of Fig. 10 shows the resulting PNLF with black crosses indicating the bin width, and the errors due to counting statistics and the uncertainty of the Ly- α LF. Due to the sharp decrease of the PNLF beyond $m_{5007} = 28.8$, we adjust our limiting accordingly, as discussed in Sect. 3.4. As the generalised function does not account for a decrease of the PNLF with magnitude, we fitted the PNLF to a maximal magnitude of $m_{\max} = 28.3$.

For a fixed parameter c_2 , we determined a distance modulus $\mu = 31.34 \pm 0.04$ with $\chi_{\text{red}}^2 = 1.3$. Allowing for a variation of the slope we fit $c_2 = 0.69 \pm 0.12$ and $\mu = 31.29 \pm 0.05$ with $\chi_{\text{red}}^2 = 0.4$. A PNLF with a steeper slope compared to M 31 (Ciardullo et al. 1989) is clearly favoured, but the distance modulus determined in the two fits is similar. Besides of the error in the best-fit, we also needed to account for further sources of error. The random uncertainty in the determination of the photometric zero-point is $\Delta Z_{[\text{OIII}]} = 0.04$. The absolute bright cut-off of the PNLF is $M^* = -4.51^{+0.02}_{-0.04}$ (Ciardullo et al. 2002). Our final distance to M 49 is thus $\mu_{\text{PNLF}} = 31.29^{+0.07}_{-0.08}$, which is in agreement with the distance modulus determined from surface brightness fluctuations (SBFs), which is $\mu_{\text{SBF}} = 31.17 \pm 0.07$ (SBFs, Mei et al. 2007). However, it does not agree with an earlier study of PNe in the centre of M 49, which determines the distance modulus to be $\mu_{\text{PNLF}} = 30.70 \pm 0.14$ (Jacoby et al. 1990). As there is only a very small overlap between this survey and ours, we are not able to conclude whether this difference in distance modulus is to be ascribed to a zero-point offset between the two photometric systems.

This leads us to the discrepancy between SBF and PNLF distances. Previous studies have generally found a discrepancy

between SBF and PNLF distances, which amounts to a mean difference of $\Delta\mu(\text{PNLF} - \text{SBF}) \approx -0.3$ (Ciardullo et al. 2002; Ciardullo 2012; Mendez 2016). SBF, as the PNLF, is a secondary distance indicator that makes use of luminosity fluctuations due to counting statistics in the individual pixels of CCDs whose amplitude is inversely proportional to the galaxy's distance (Tonry & Schneider 1988). Both SBF and PNLF distances are calibrated based on Cepheid distances (Ciardullo et al. 2002; Tonry et al. 2001). Several explanations for the discrepancy are discussed in Ciardullo (2012), arguing that it is likely a combination of multiple small effects like zero-point offsets of the two methods and different extinction due to dust in different galaxy types.

The offsets in distance moduli neither correlate with absolute galaxy magnitude, nor with galaxy colour, however a small correlation is found between offset and SBF distance modulus (Ciardullo et al. 2002). There are multiple factors that could be responsible for this correlation. It could be due to uncertainties in the measurement in relatively nearby spirals ($\mu_{\text{SBF}} \sim 29-30$, Ciardullo 2012), or to contamination by foreground intracluster stars or background galaxies (Ciardullo et al. 2002). As we detail in Sect. 3.5.2, Ly- α emitters at redshift $z = 3.1$ can mimic the unresolved [OIII] emission of PNe and cannot be distinguished from PNe solely based on photometric surveys. This contamination affects galaxies with distance moduli larger than $\mu_{5007} \geq 30.5$, and can bias the empirical PNLF towards brighter magnitudes due to the presence of Ly- α emitters brighter than the PNLF cut-off. By comparing the empirical PNLF with the contribution of the Ly- α LF scaled by filter area and depth, the overluminous sources in the left panel of Fig. 10 are clearly consistent with Ly- α -emitting background galaxies. Further validation must await the spectroscopic follow-up of these objects.

A recent MUSE study of the star-forming disc galaxy NGC 628 drew the attention to another source of contamination: supernova remnants, that also appear as unresolved [OIII]-emitting objects (Kreckel et al. 2017). However, these objects

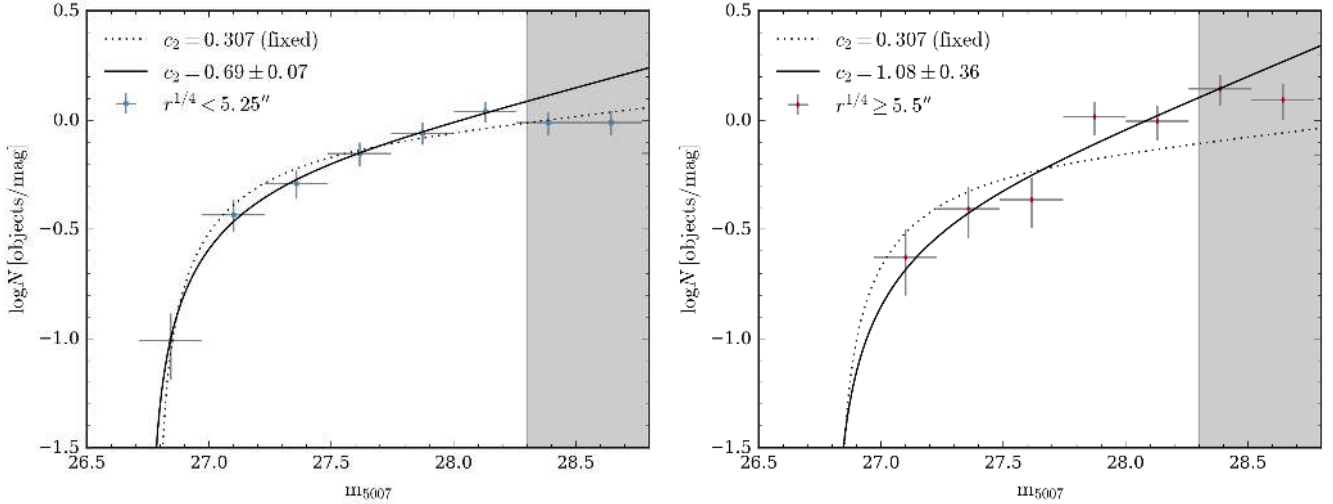


Fig. 11. PNLF of the completeness-corrected PN sample in two radial bins. *Left panel:* PN sample in the inner halo ($r^{1/4} < 5.25''$); *right panel:* sample in the outer halo ($r^{1/4} \geq 5.25''$). The error bars along the y -axis account for the Poissonian error and the x -errors for the bin width. The solid lines show the fits to the PNLF allowing for variation in the parameter c_2 while the dashed lines show the fits with a fixed $c_2 = 0.307$ (Ciardullo et al. 1989). As in Fig. 10, the grey region denotes the magnitude range in which the PNLF might be affected by incompleteness.

are predominantly expected in star-forming galaxies as the [OIII] emission from these SN remnants comes from the interaction of the SN blast wave with the circumstellar medium of the progenitor. This is relevant for core-collapse SNe in spiral galaxies which do not occur in ETG-like galaxies like M 49 (e.g. Cappellaro et al. 1999).

We are aware that the PNLF distance determination in M 87 (L13) still finds a 0.3 mag discrepancy between the PNLF and SBF distance moduli of M 87, also for spectroscopically confirmed PN sample (Longobardi et al. 2015a). As Ly- α emitters were identified in the spectroscopic follow-up, any overluminous Ly- α emitter biasing the PNLF cut-off to brighter magnitudes is expected to have been removed from the PN sample.

6. Tracing halo variation with PNe

In Sect. 4 we found evidence for two different PN populations in the inner and outer halo based on a variation of the α -parameter. We want to investigate whether these differences are also reflected in the PNLF. The PNLF does not only serve as a distance indicator, but furthermore provides insights into the underlying stellar populations, which influence its morphology at fainter magnitudes than the bright cut-off.

6.1. The PNLF morphology in the inner and outer halo

We first divided the PN sample into two concentric elliptical bins, indicated by the grey line in Fig. 7 at $r^{1/4} = 5.25$. The inner sample is characterised by a density profile that decreases steeply with radius, and contains 517 PNe, whereas the outer sample has a shallower number density profile and contains 197 objects (see also Sect. 4). We computed the completeness-corrected PNLF in each bin, normalising by the total number of objects for better comparison and again fit the generalised PNLF. The resulting profiles are shown in Fig. 11. For comparison we also show the PNLF with a fixed $c_2 = 0.307$, which is clearly disfavoured in both bins. The PNLF in the outer bin is less well fit by the generalised function than the one in the inner bin. The fitted distance moduli are $\mu_{\text{PNLF,inner}} = 31.27 \pm 0.02$

and $\mu_{\text{PNLF,outer}} = 31.31 \pm 0.05$, which agree with the distance modulus determined in the previous section.

In the outer regions of the halo, the slope of the PNLF is steeper ($c_{2,\text{outer}} = 1.08 \pm 0.36$) than in the inner region ($c_{2,\text{inner}} = 0.69 \pm 0.07$). Empirically, one would thus expect an older underlying stellar population in the outer halo compared to the inner halo. This seems counterintuitive, given the colour gradient towards bluer colour and the general understanding of halo growth through accretion of smaller, younger systems (Oser et al. 2012; Cooper et al. 2013). In the following section we investigate the properties of the PNLF in the inner halo.

6.2. PNLF variation in the inner halo

As M 49's halo is rich in substructure (Janowiecki et al. 2010, C15), we next investigate the azimuthal variation of the PNLF in the inner halo. We therefore divide the halo into four quadrants, such that the positive and negative minor and major axes are enclosed respectively, as shown in Fig. 13. The quadrants are denominated by their position with respect to M 49's centre (north, west, east, south). We calculate the completeness-corrected PNLF in each quadrant and normalise it by the total number of PN in that quadrant. The resulting profiles are shown in Fig. 12. We again fitted the generalised PNLF to each profile.

While the PNLF in the northern, southern, and western quadrants have similar slopes ranging from $c_2 = 0.87 \pm 0.37$ in the north to $c_2 = 0.70 \pm 0.15$ in the south, the slope of the PNLF in the eastern quadrant is significantly flatter, being $c_2 = 0.21 \pm 0.20$, even shallower than the slope of the Ciardullo-PNLF. Compared to the other quadrants, the bright end of the PNLF in the east is populated by more objects. This drives the flattening of the PNLF in the inner halo, which we described in the previous section. If this flattening is related to a younger stellar population, it likely points towards an accretion event. No substructure is found in deep broad-band photometric studies (Janowiecki et al. 2010) in this quadrant, which could be associated to the PNLF variation. However, the spatial proximity to the trail of the accreted dIrr galaxy VCC 1249, which could well extend further into the eastern quadrant, argues for a relation between the flat PNLF and this accretion event.

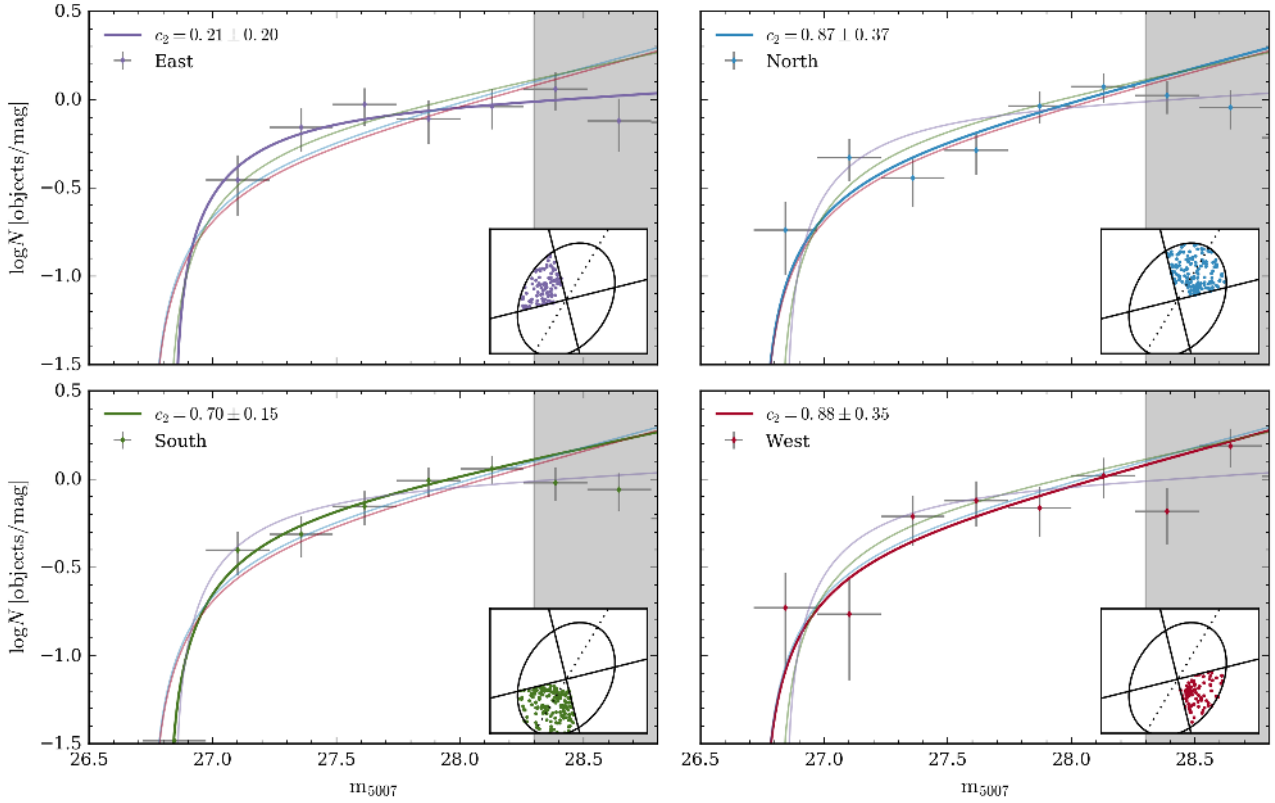


Fig. 12. PNLF variation in the inner bin in four quadrants. Each panel shows the observed PNLF (data points and error bars) and the corresponding fit for the quadrant indicated in the inset.

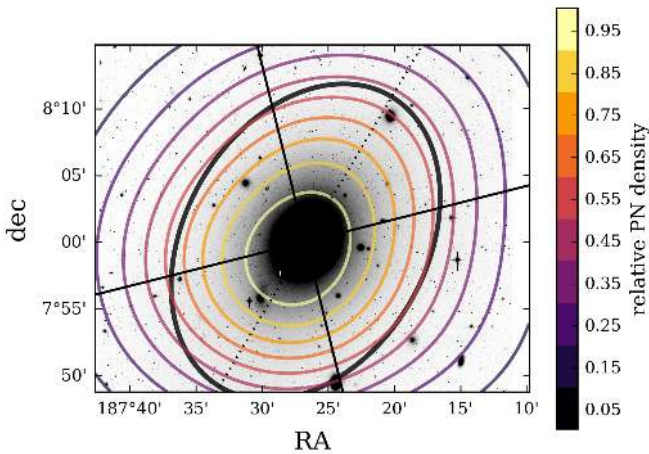


Fig. 13. NGVS g -band image of M49 (from Arrigoni Battaia et al. 2012) with 2D contours of the relative PN density superimposed. The black ellipse denotes the major-axis transition radius from the inner to the outer halo at $730''$ as defined in Sect. 4, the dashed line indicates the major axis and the solid lines the borders of the quadrants as defined in Sect. 6.

6.3. 2D number density map

We next evaluated whether we can identify any substructure in the 2D PNe density distribution. We therefore performed a kernel density estimate (KDE) with a Gaussian kernel using `scikit-learn` (Pedregosa et al. 2011). The kernel bandwidth was chosen such that no artificial overdensities are introduced due to the masked regions in the centre. The resulting density

contours overlotted on the NGVS g -band image are shown in Fig. 13. This fig. also shows the borders of the quadrants defined in the previous section, as well as the boundary between the inner and outer halo. Due to the large bandwidth we were not able to resolve individual structures. The PN-contours along the north of the major axis have a similar position angle and ellipticity as the isophotes from broad-band studies, in the south are flattened and denser. This spatial squashing coincides with region of interaction with VCC 1249.

7. Discussion

Hydrodynamical cosmological simulations such as the Illustris simulations (Vogelsberger et al. 2014) predict that accretion and mergers will deposit significant amounts of tidally stripped stars in the outer regions of galaxies (Pillepich et al. 2015). Because the dynamical timescales in galaxy outskirts, at 50–150 kpc radii, are of the order of 2 Gyr, this predictions can be tested by looking observationally for unrelaxed dynamical structures at these radii. This motivates the investigation in this paper of the observational evidence for substructures, environmental effects and IGL around the giant Virgo galaxy M49.

7.1. Substructure in M49

Recent deep broad-band photometric studies have revealed an intricate system of stellar substructure in M49's halo. Janowiecki et al. (2010) fit Sérsic and double-deVaucouleurs profiles to their V -band photometry and subtract the resulting galaxy model from the images in order to identify substructures. They find a system of diffuse shells, mainly along the major

axis of the galaxy. Furthermore, there are two plumes to the south and in the north-east of the galaxy, the latter running through the dwarf galaxy VCC 1254. There might be a connection between the south plume and the inner shell system. This plume is also closely located to the dwarf irregular (dIrr) galaxy VCC 1249, whose properties will be discussed later in this section. The colours of the substructures that were identified by Janowiecki et al. (2010) were measured by Mihos et al. (2013). Their measurement of the global colour trend in the halo of M 49 was already discussed in Sect. 4. The starforming companions of M 49 (VCC 1249 and VCC 1205) clearly stand out due to their bluer $B - V$ colour. The inner shells cannot be identified in the colour map, as they are too close to the bright and red main halo of the galaxy. However, the extended debris shell in the north-west can be identified in the colour map. It is ~ 0.07 mag redder than the remainder of the halo at this radius, indicating that the shell is a remnant of a disruptive accretion event.

The interaction between the dIrr galaxy VCC 1249 and M 49 has come to the attention after the detection of an H I cloud displaced from the dwarf towards M 49 (Krishna Kumar & Thonnard 1983). Follow-up VLA observations of this cloud by McNamara et al. (1994) revealed a debris trail between the dIrr and M 49. A multi-wavelength analysis of this region (Arrigoni Battaia et al. 2012) including near-UV data as well as optical imaging, H α and spectroscopy comes to the conclusion that star formation in VCC 1249 has been quenched. Due to ram pressure stripping and tidal interaction H I gas has been removed from the dIrr core. Star formation remains active in the H I cloud.

Spatially coinciding with this accretion event, we observe denser PN contours south-east of M 49's centre (Sect. 6.3). Having evaluated the PNLf in different quadrants, we however do not find a significant change in the PNLf morphology in this region (Sect. 6.2). A significant difference in the PNLf slope is indeed found in the adjacent eastern quadrant. The flattening of the PNLf slope can have multiple origins, being driven by either an overabundance of bright to medium luminosity PNe or a lack of fainter PNe. Based on Fig. 12 we assume that the presence of additional medium luminosity PNe ($27.2 \leq m_{5007} \leq 27.7$) compared to the general halo population is driving the flattening of the PNLf. The presence of these bright objects could very well be related to the accretion of VCC 1249, as the shedding of tidal debris after its pericentre passage can lead to a wider distribution of stars (and therefore PNe) than inferred from the distribution of the light (e.g., Amorisco 2015). The validation of this claim will be one of the aims of the spectroscopic follow-up survey of this data, with which we expect to be able to identify accretion events based on their signatures in the kinematic phase-space.

7.2. The effect of environment: a comparison to M 87

M 87 has been a milestone for this type of PN-surveys in the Virgo cluster. With the spectroscopic follow-up of the deep photometric PN-survey (L13), Longobardi et al. (2015a) were able to kinematically separate the stellar halo and intracluster light and furthermore found evidence for a late accretion event in M 87's velocity phase-space (Longobardi et al. 2015b).

We first compared the properties of the PN number density profiles in the two galaxies. The morphology of the number density profiles is very similar, both closely following the stellar light (K09) in the inner galaxy halos and then flattens at larger radii. In both galaxies, a two-component model is fit that allows for different α -parameters of the galaxy PN and the PN associated with the ICL/IGL. We scaled M 87's α -parameters by a

factor of 0.54, as they were calculated assuming a distance modulus of $\mu_{5007} = 30.8$ (L13) instead of $\mu_{\text{SBF}} = 31.17$ (Mei et al. 2007), resulting in

$$\begin{aligned} - \alpha_{2.5,\text{halo}}^{\text{M87}} &= (5.94_{-0.21}^{+0.17}) \times 10^{-9} \text{ PN } L_{\odot,\text{bol}}^{-1} \text{ for the halo component,} \\ &\text{and} \\ - \alpha_{2.5,\text{ICL}}^{\text{M87}} &= (1.78_{-0.72}^{+0.60}) \times 10^{-8} \text{ PN } L_{\odot,\text{bol}}^{-1} \text{ for the ICL component} \\ &\text{(L13).} \end{aligned}$$

The ratio between the two parameters is $\alpha_{2.5,\text{ICL}}/\alpha_{2.5,\text{halo}} = 3$. In the photometric study, the contribution of the ICL was expected to be constant $\mu_V = 27.7$ mag arcsec $^{-2}$. In M 49, we assume that the contribution from the IGL is $\mu_V = 28.0$ mag arcsec $^{-2}$. For reference M 49's α -parameters as determined in Sect. 4 of this paper are

$$\begin{aligned} - \alpha_{2.5,\text{inner}}^{\text{M49}} &= (3.20 \pm 0.43) \times 10^{-9} \text{ PN } L_{\odot,\text{bol}}^{-1} \text{ for the inner component (halo), and} \\ - \alpha_{2.5,\text{outer}}^{\text{M49}} &= (1.03 \pm 0.22) \times 10^{-8} \text{ PN } L_{\odot,\text{bol}}^{-1} \text{ for the outer component (IGL).} \end{aligned}$$

The α -parameter in the main halo of M 87 is higher compared to the one in M 49, while the ICL and IGL have consistent α -values within the errors.

The halo PNLf of M 87 is steeper than what is expected based on the analytic PNLf from Ciardullo et al. (1989), which motivated the introduction of the generalised analytic PNLf in L13. The distance modulus and the slope are fit to be $\mu = 30.73$ and $c_2 = 1.17$. The determined distance modulus is ~ 0.4 mag brighter than the one determined using SBFs (Mei et al. 2007). In Longobardi et al. (2015a), the slope of the halo and ICL PNLfs were determined based on the kinematically separated populations, leading to $c_{2,\text{halo}} = 0.72$ and $c_{2,\text{ICL}} = 0.66$. The PNLf of the ICL shows a dip 1–1.5 mag from the bright cut-off, which is seen in star-forming systems. There is little variation of the PNLf with radius. In contrast to this, we find differences in the PNLf slope in different regions of M 49's halo. The slope of the PNLf in the entire sample is also steeper ($c_2 = 0.69 \pm 0.12$) than the analytic PNLf from Ciardullo et al. (1989), which further corroborates the empirical trend of steepening PNLfs from star-forming to old metal-rich populations (L13; Ciardullo et al. 2004; Ciardullo 2010). We believe that the flat PNLf in the inner halo of M 49 is driven by the excess of bright to medium-luminosity planetaries in the eastern quadrant.

We spatially associate this excess with the tail of the accretion event of VCC 1249, but note that there is no overdensity that can be related with it in the broad-band photometric surveys of M 49's halo (Janowiecki et al. 2010; Capaccioli et al. 2015). As identified in Longobardi et al. (2015b), M 87's kinematic PN phase-space reveals signatures of a recent accretion event, also termed as M 87's crown. However, the PNLf of the crown in M 87 does not show signs of variation from the halo PNLf. The nature of the accreted system is very different from what is observed for the VCC 1249 – M 49 interaction. Reflecting the environment of Virgo's subcluster A, the infalling system was devoid of gas. The subcluster B at whose centre M 49 resides mainly consists of star-forming galaxies. Thus the infall of a gas-rich, star-forming galaxy is more likely to be observed in the subcluster B.

7.3. M 49 and its environment: the intragroup light in the Virgo subcluster B

Combining our study of individual tracers (PNe) with broad-band photometric observations of M 49 and its environment

allows us to model the PN populations in M49's halo as a two-component system that consists of an inner Sérsic-like halo and a flat outer component with a constant surface brightness (see Sect. 4.4). Our best-fit model is characterised by the α -parameters of the respective components, which we re-stated in Sect. 7.2 above.

By applying the same concept to the colour profile (Mihos et al. 2013), we are able to derive a relation between the α -parameter and the $(B - V)$ colour at each radius: M49's α -parameter increases with decreasing colour. The best-fit colour model consists of an inner component with a radially dependent colour profile with gradient $\Delta_i = (-1.0 \pm 0.4) \times 10^{-4}$ mag arcsec $^{-1}$ and $(B - V)_i = (B - V)_{\text{inner}}(r = 0) = 0.96 \pm 0.01$ and an outer component of constant colour $(B - V)_{\text{outer}} = 0.25 \pm 0.11$. The comparison with the most recent hydrodynamical, cosmological simulations, shows that the Sérsic component and its mild colour gradient of $\nabla(B - V)_{2-4r_c} = -0.13$ mag dex $^{-1}$ are consistent with the hierarchical assembly of ETGs (Cook et al. 2016). In fact, the colour profiles measured in the Illustris simulation have an average $(g - r)$ colour gradient of $\nabla(g - r)_{2-4r_c} \approx -0.1$ mag dex $^{-1}$ (Cook et al. 2016) with a scatter of $\sigma \approx 0.08$ mag dex $^{-1}$. This is much shallower than the global gradient observed in M49 that ranges from $\nabla(B - V)_{2-4r_c} = -0.3$ mag dex $^{-1}$ in the inner halo to $\nabla(B - V)_{4-8r_c} = -0.8$ mag dex $^{-1}$ in the outer halo, thus supporting the presence of an additional component.

The shallow, blue, outer component is likely due to a contribution of a smooth IGL that is superposed onto the Sérsic galaxy halo. This result is consistent with the extended photometry from the Burrell Schmidt deep Virgo survey (Mihos et al. 2017) and the VEGAS survey (C15). Because Mihos et al. (2017)'s morphological classification of ICL/IGL is based on the luminosity fraction that is either in filamentary or in clumpy structures, in addition to an azimuthally smooth spheroid, the smooth blue IGL around M49 would not fall in this classification and hence their different conclusion on the presence of IGL around M49. We also note that the footprint of the Burrell Schmidt survey does not extend to the south of M49, where the outer boundary of the external envelope is most elongated (see Fig. 6 in C15).

As the outer halo of M49 is observed to be smooth (C15, Mihos et al. 2017) we would expect the component to have already started to relax. As the precession time at these radii is about 5 Gyr, following the simple stellar population models of Bruzual & Charlot (2003) applied to M49 in Mihos et al. (2013), we expect this population to be quite metal-poor ($[\text{Fe}/\text{H}] \leq -2$). Similar to the analysis in M87 by Longobardi et al. (2015a), we are planning to carry out a spectroscopic follow-up of the PN-survey presented in this paper. This will enable us to assess the degree of relaxation of the outer component, which points towards its evolutionary history. Based on their velocity phase-space properties we will also be able to kinematically disentangle the halo and IGL populations.

8. Summary and conclusions

We present a deep narrow-band survey of the bright ETG M49 using Subaru's Suprime-Cam in order to identify and analyse the PN population therein. The survey's extent and depth is unprecedented for M49. Down to a limiting magnitude of $m_{5007,\text{lim}} = 28.8$ and covering a radial range of 155 kpc from the galaxy's centre, we identify a PNLF-complete sample of 624 PNe using automated detection techniques. The selection criteria are based on the fact the PNe have a bright [OIII] and no continuum

emission and that they appear as point-like at extragalactic distances. Using a simulated PN population, we are able to account for detection and colour incompleteness.

The radial PN number density profile follows the broad-band surface brightness distribution to a radius of $r = 730''$, equivalent to $r = 60$ kpc and then shows flattening with respect to the stellar surface brightness profile. This is consistent with a two-component model that accounts for a Sérsic distribution of halo PNe in the inner region and a shallower population of IGL PNe at larger radii. The α -parameter of this IGL population signifies a 3.2 times higher specific frequency of PNe in the IGL compared to the main galaxy halo, which is similar to what was observed in Virgo's BCG M87 (L13).

The PNLF is as an important diagnostic tool for the properties of the global PN population of M49's halo as well as for variation therein. First, due to accurate account for contamination by Ly- α emitting background galaxies at $z = 3.1$, we are able to determine a PNLF distance modulus that agrees with the one determined using the SBF technique, which is a first for a galaxy at this distance. Second, the PNLF slope varies in the inner halo of M49, due to additional bright PNe in one quadrant. Whether these PNe are related to the accretion of VCC 1249 will be one of the aims of the planned spectroscopic follow-up. We will also be able to disentangle the halo and intragroup populations by studying their kinematics separately.

While both M49 and M87 are massive and bright early-type galaxies in the Virgo cluster, their PN populations have different properties, reflecting the different environments in which they reside. M87 in Virgo's most dense environment, the subcluster A, is surrounded by ICL with a higher specific frequency compared to the IGL around M49 in Virgo's subcluster B. Both galaxies are undergoing or have undergone recent accretion. The fact that M87's accreted companion did not contain any gas, while M49 has multiple star-forming companions reflects the different environments in which the halos of these ETGs grew.

Acknowledgements. The authors thank the on-site Subaru staff for their support, Patrick Durrell for the provision of the NGVS number density profiles in M49, and Fabrizio Arrigoni Battaia for the NGVS g -band image of M49. This research made use of Astropy, a community-developed core Python package for Astronomy (Astropy Collaboration et al. 2013). This publication made use of data products from the Two Micron All Sky Survey (University of Massachusetts and the Infrared Processing and Analysis Center/California Institute of Technology), funded by the National Aeronautics and Space Administration and the National Science Foundation. The authors thank the referee for the constructive comments and the careful reading of the manuscript.

References

- Aguerri, J. A. L., Gerhard, O. E., Arnaboldi, M., et al. 2005, *AJ*, 129, 2585
- Amorisco, N. C. 2015, *MNRAS*, 450, 575
- Arnaboldi, M., Freeman, K. C., Mendez, R. H., et al. 1996, *ApJ*, 472, 145
- Arnaboldi, M., Freeman, K. C., Gerhard, O., et al. 1998, *ApJ*, 507, 759
- Arnaboldi, M., Aguerri, J. A. L., Napolitano, N. R., et al. 2002, *AJ*, 123, 760
- Arnaboldi, M., Freeman, K. C., Okamura, S., et al. 2003, *AJ*, 125, 514
- Arrigoni Battaia, F., Gavazzi, G., Fumagalli, M., et al. 2012, *A&A*, 543, A112
- Astropy Collaboration, Robitaille, T. P., Tollerud, E. J., et al. 2013, *A&A*, 558, A33
- Bertin, E., & Arnouts, S. 1996, *A&AS*, 117, 393
- Binggeli, B., Tammann, G. A., & Sandage, A. 1987, *AJ*, 94, 251
- Binggeli, B., Popescu, C. C., & Tammann, G. A. 1993, *A&AS*, 98, 275
- Boselli, A., Voyer, E., Boissier, S., et al. 2014, *A&A*, 570, A69
- Bruzual, G., & Charlot, S. 2003, *MNRAS*, 344, 1000
- Buzzoni, A., Arnaboldi, M., & Corradi, R. L. M. 2006, *MNRAS*, 368, 877
- Caon, N., Capaccioli, M., & D'Onofrio, M. 1994, *A&AS*, 106, 199
- Capaccioli, M., Spavone, M., Grado, A., et al. 2015, *A&A*, 581, A10 (C15)
- Cappellari, M. 2016, *ARA&A*, 54, 597
- Cappellari, E., Evans, R., & Turrato, M. 1999, *A&A*, 351, 459

- Castro-Rodríguez, N., Arnaboldi, M., Aguerri, J. A. L., et al. 2009, *A&A*, 507, 621
- Ciardullo, R. 2010, *PASA*, 27, 149
- Ciardullo, R. 2012, *Ap&SS*, 341, 151
- Ciardullo, R., Jacoby, G. H., Ford, H. C., & Neill, J. D. 1989, *ApJ*, 339, 53
- Ciardullo, R., Jacoby, G. H., Feldmeier, J. J., & Bartlett, R. E. 1998, *ApJ*, 492, 62
- Ciardullo, R., Feldmeier, J. J., Jacoby, G. H., et al. 2002, *ApJ*, 577, 31
- Ciardullo, R., Durrell, P. R., Laychak, M. B., et al. 2004, *ApJ*, 614, 167
- Ciardullo, R., Gronwall, C., Wolf, C., et al. 2012, *ApJ*, 744, 110
- Coccatto, L., Gerhard, O., Arnaboldi, M., et al. 2009, *MNRAS*, 394, 1249
- Coccatto, L., Arnaboldi, M., & Gerhard, O. 2013, *MNRAS*, 436, 1322
- Colless, M., Ellis, R. S., Taylor, K., & Hook, R. N. 1990, *MNRAS*, 244, 408
- Cook, B. A., Conroy, C., Pillepich, A., Rodriguez-Gomez, V., & Hernquist, L. 2016, *ApJ*, 833, 158
- Cooper, A. P., D'Souza, R., Kauffmann, G., et al. 2013, *MNRAS*, 434, 3348
- Cortesi, A., Arnaboldi, M., Coccatto, L., et al. 2013a, *A&A*, 549, A115
- Cortesi, A., Merrifield, M. R., Coccatto, L., et al. 2013b, *MNRAS*, 432, 1010
- Côté, P., McLaughlin, D. E., Cohen, J. G., & Blakeslee, J. P. 2003, *ApJ*, 591, 850
- Crnojević, D., Ferguson, A. M. N., Irwin, M. J., et al. 2013, *MNRAS*, 432, 832
- Crnojević, D., Sand, D. J., Spekkens, K., et al. 2016, *ApJ*, 823, 19
- Cui, W., Murante, G., Monaco, P., et al. 2014, *MNRAS*, 437, 816
- Daddi, E., Renzini, A., Pirzkal, N., et al. 2005, *ApJ*, 626, 680
- Dopita, M. A., Jacoby, G. H., & Vassiliadis, E. 1992, *ApJ*, 389, 27
- Douglas, N. G., Arnaboldi, M., Freeman, K. C., et al. 2002, *PASP*, 114, 1234
- Durrell, P. R., Côté, P., Peng, E. W., et al. 2014, *ApJ*, 794, 103
- Feldmeier, J. J., Ciardullo, R., & Jacoby, G. H. 1998, *ApJ*, 503, 109
- Feldmeier, J. J., Ciardullo, R., Jacoby, G. H., & Durrell, P. R. 2003, *ApJS*, 145, 65
- Feldmeier, J. J., Ciardullo, R., Jacoby, G. H., & Durrell, P. R. 2004, *ApJ*, 615, 196
- Ferrarese, L., Côté, P., Cuillandre, J.-C., et al. 2012, *ApJS*, 200, 4
- Gawiser, E., Francke, H., Lai, K., et al. 2007, *ApJ*, 671, 278
- Gonzalez, A. H., Zabludoff, A. I., & Zaritsky, D. 2005, *ApJ*, 618, 195
- Greggio, L., & Renzini, A. 2011, *Stellar Populations, A User Guide from Low to High Redshift* (Wiley-VCH-Verlag)
- Gronwall, C., Ciardullo, R., Hickey, T., et al. 2007, *ApJ*, 667, 79
- Hammer, F., Flores, H., Lilly, S. J., et al. 1997, *ApJ*, 481, 49
- Hargis, J. R., & Rhode, K. L. 2014, *ApJ*, 796, 62
- Henize, K. G., & Westerlund, B. E. 1963, *ApJ*, 137, 747
- Hogg, D. W., Cohen, J. G., Blandford, R., & Pahre, M. A. 1998, *ApJ*, 504, 622
- Hui, X., Ford, H. C., Freeman, K. C., & Dopita, M. A. 1995, *ApJ*, 449, 592
- Irwin, J. A., & Sarazin, C. L. 1996, *ApJ*, 471, 683
- Jacoby, G. H. 1989, *ApJ*, 339, 39
- Jacoby, G. H., Ciardullo, R., & Ford, H. C. 1990, *ApJ*, 356, 332
- Janowiecki, S., Mihos, J. C., Harding, P., et al. 2010, *ApJ*, 715, 972
- Kormendy, J., Fisher, D. B., Cornell, M. E., & Bender, R. 2009, *ApJS*, 182, 216
- Kreckel, K., Groves, B., Bigiel, F., et al. 2017, *ApJ*, 834, 174
- Krishna Kumar, C., & Thonnard, N. 1983, *AJ*, 88, 260
- Longobardi, A., Arnaboldi, M., Gerhard, O., et al. 2013, *A&A*, 558, A42 (L13)
- Longobardi, A., Arnaboldi, M., Gerhard, O., & Hanuschik, R. 2015a, *A&A*, 579, A135
- Longobardi, A., Arnaboldi, M., Gerhard, O., & Mihos, J. C. 2015b, *A&A*, 579, L3
- McConnachie, A. W., Irwin, M. J., Ibata, R. A., et al. 2009, *Nature*, 461, 66
- McNamara, B. R., Sancisi, R., Henning, P. A., & Junor, W. 1994, *AJ*, 108, 844
- Mei, S., Blakeslee, J. P., Côté, P., et al. 2007, *ApJ*, 655, 144
- Mendez, R. H. 2016, IAU Symp., 323, in press [[arXiv:1610.08625](https://arxiv.org/abs/1610.08625)]
- Méndez, R. H., Riffeser, A., Kudritzki, R.-P., et al. 2001, *ApJ*, 563, 135
- Merrett, H. R., Merrifield, M. R., Douglas, N. G., et al. 2006, *MNRAS*, 369, 120
- Mihos, J. C., Harding, P., Feldmeier, J., & Morrison, H. 2005, *ApJ*, 631, L41
- Mihos, J. C., Harding, P., Rudick, C. S., & Feldmeier, J. J. 2013, *ApJ*, 764, L20
- Mihos, J. C., Harding, P., Feldmeier, J. J., et al. 2017, *ApJ*, 834, 16
- Miyazaki, S., Komiyama, Y., Sekiguchi, M., et al. 2002, *PASJ*, 54, 833
- Newville, M., Stensitzki, T., Allen, D. B., & Ingargiola, A. 2014, LMFIT: Non-Linear Least-Square Minimization and Curve-Fitting for Python
- Oser, L., Ostriker, J. P., Naab, T., Johansson, P. H., & Burkert, A. 2010, *ApJ*, 725, 2312
- Oser, L., Naab, T., Ostriker, J. P., & Johansson, P. H. 2012, *ApJ*, 744, 63
- Pedregosa, F., Varoquaux, G., Gramfort, A., et al. 2011, *J. Mach. Learn. Res.*, 12, 2825
- Pillepich, A., Madau, P., & Mayer, L. 2015, *ApJ*, 799, 184
- Pota, V., Forbes, D. A., Romanowsky, A. J., et al. 2013, *MNRAS*, 428, 389
- Renzini, A., & Buzzoni, A. 1986, in *Spectral Evolution of Galaxies*, eds. C. Chiosi & A. Renzini, *Astrophys. Space Sci. Lib.*, 122, 195
- Rudick, C. S., Mihos, J. C., & McBride, C. 2006, *ApJ*, 648, 936
- Rudick, C. S., Mihos, J. C., Harding, P., et al. 2010, *ApJ*, 720, 569
- Schechter, P. 1976, *ApJ*, 203, 297
- Schindler, S., Binggeli, B., & Böhringer, H. 1999, *A&A*, 343, 420
- Sérsic, J. L. 1963, *Boletín de la Asociación Argentina de Astronomía La Plata Argentina*, 6, 41
- Somerville, R. S., Lee, K., Ferguson, H. C., et al. 2004, *ApJ*, 600, L171
- Steinmetz, M., & Navarro, J. F. 2002, *New Astron.*, 7, 155
- Teplitz, H. I., Malkan, M. A., Steidel, C. C., et al. 2000, *ApJ*, 542, 18
- Theuns, T., & Warren, S. J. 1997, *MNRAS*, 284, L11
- Thomas, J., Saglia, R. P., Bender, R., et al. 2005, *MNRAS*, 360, 1355
- Tonry, J., & Schneider, D. P. 1988, *AJ*, 96, 807
- Tonry, J. L., Dressler, A., Blakeslee, J. P., et al. 2001, *ApJ*, 546, 681
- Usher, C., Forbes, D. A., Brodie, J. P., et al. 2012, *MNRAS*, 426, 1475
- van Dokkum, P. G., Franx, M., Kriek, M., et al. 2008, *ApJ*, 677, L5
- Vogelsberger, M., Genel, S., Springel, V., et al. 2014, *MNRAS*, 444, 1518
- White, S. D. M., & Frenk, C. S. 1991, *ApJ*, 379, 52
- Zibetti, S., White, S. D. M., Schneider, D. P., & Brinkmann, J. 2005, *MNRAS*, 358, 949

Appendix A: Catalogue extraction

A.1. Extraction of point-like emission-line objects

We extracted emission-line objects using the object detection algorithm SExtractor (Bertin & Arnouts 1996) in dual-image mode. Objects were detected if the flux value in at least 20 adjacent pixels is higher than $1.2 \times \sigma_{\text{rms}}$ in the on-band image. We chose an aperture radius of 12 pixels, since this is the smallest aperture in which we can recover the magnitudes of a simulated emission-line population (see Fig. A.1). The detection in dual-image mode was carried out on the on-band image and the extracted aperture magnitudes are denoted with m_n . In order to determine the colour of the emission-line objects, the broad-band magnitudes m_b were extracted in the same apertures as on the narrow-band image. The colour is defined as $m_n - m_b$.

In order to determine the limiting magnitude of our sample, we simulated a synthetic point-like population onto the on-band image using the IRAF task mkobjects. The synthetic population follows a PNLF as detailed in Ciardullo et al. (1989, see also Sect. 5) and the objects have a Gaussian PSF profile as detailed in Sect. 2.2. The limiting magnitude is defined as the magnitude at which the recovery fraction of the simulated objects drops below 50%. The limiting AB magnitude of the on-band image is $m_{n,\text{lim}} = 26.8$ or $m_{5007,\text{lim}} = 29.3$ (see also Col. 3 of Table A.1).

A.2. Masking of bad or noisy regions

After identifying emission-line objects on the images, the image regions which were affected by dithering or saturation are masked on the on- and off-band images. Dithering leads to different exposure depths at the image edges. Due to the combination of the 10 Suprime Cam CCDs, the same effect also affects columns at the borders of the individual CCDs. In order to mask regions with a high background value (e.g. due to charge transfer or saturated stars) we used the rms-background map created by SExtractor and create a pixel-mask with all values higher than 1.5 times the median background. We also excluded objects within a major-axis radius of $r_{\text{major}} = 159''$, corresponding to a physical distance of 13 kpc from the galaxy's centre, where the background due to the galaxy's light is higher than the threshold defined above. This reduces the survey area by 4% to 0.244 deg^2 .

A.3. Colour selection

We selected PN candidates based on their position on the m_n versus $m_n - m_b$ CMD. Candidates were objects with a colour excess $m_n - m_b < -1$ that are brighter than the limiting AB magnitude in the narrow band $m_{n,\text{lim}} = 26.8$, which corresponds to $m_{5007,\text{lim}} = 29.3$. The colour excess corresponds to an equivalent width $EW_{\text{obs}} = 110 \text{ \AA}$ (Teplitz et al. 2000) and was chosen in order to limit contamination from background galaxies (see discussion in Sect. 3.5.2).

To evaluate the contamination by faint stellar sources that fall below the adopted colour excess due to photometric errors, we simulated a continuum population onto the on- and off-band images and calculate the 99% and 99.9% limits based on the extracted CMD of the population. Below these limits, the probability of detecting stars was reduced to the 1% and 0.1% level respectively. Objects with colour-excess above the 99.9% limit are not considered for further analysis. The CMD with the selection criteria overplotted is shown in Fig. 1. [OIII] sources for which no broad-band magnitude can be measured are assigned a magnitude of $m_b = 28.7$, which corresponds to the flux from an

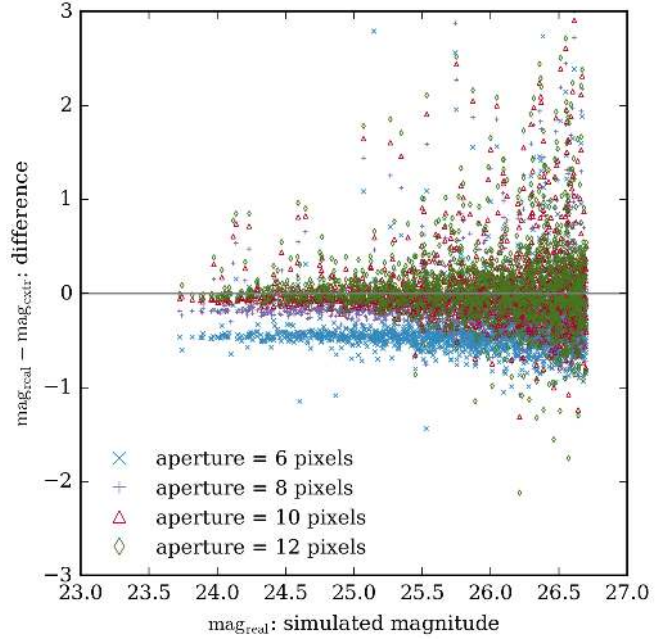


Fig. A.1. Recovery of the input magnitudes of a simulated emission-line population using different SExtractor aperture sizes.

[OIII] emission of $m_n = m_{n,\text{lim}}$ observed through a broad-band V filter (Theuns & Warren 1997). These sources are located on the diagonal line in Fig. 1.

A.4. Point-like versus extended sources

In order to distinguish point-like sources from extended ones (e.g. background galaxies or other extended objects with strong [OIII] emission), we again first considered the simulation of the PNe on the on-band image and analyse their light distribution. Based on the simulated population, we considered sources as point-like if they satisfied the following two criteria: these sources (i) have a half-light radius of $1 < R_h < 3.5$ pixel, where the upper limit corresponds to the 95%-percentile of the simulated population, and (ii) they fall in the region where the difference between m_n and m_{core} is within the 95%-limits of the simulated population. The core magnitude m_{core} was measured in a fixed circular aperture with a radius of four pixels at the same position of the main detection. For point-like objects, the difference between the two magnitudes is expected to be constant as a function of magnitude, for extended sources it varies. The results of this test are shown in Fig. 2. The objects which fulfil these criteria along with the ones detailed in the previous section are indicated in the CMD of Fig. 1.

A.5. Catalogue completeness

As we selected PN-candidates on flux-ratio-based criteria, we might not have detected PNe that fell below the flux-threshold due to photometric errors. In order to quantify the detection incompleteness, we simulated a PN-population onto the unmasked regions of the on-band image and determined how many sources we retrieved as a function of magnitude. For sources brighter than the limiting magnitude, the average detection completeness was 80%. The detection completeness as a function of magnitude is displayed in Table A.1. We then used the simulated population brighter than the limiting magnitude to determine the

Table A.1. Photometric completeness: colour completeness c_{colour} and detection completeness $c_{\text{detection}}$ for a range of narrow-band magnitudes m_n .

m_n [mag]	c_{colour}	$c_{\text{detection}}$
23.97	0.80	0.92
24.23	0.87	1.00
24.48	0.84	0.83
24.74	0.84	0.90
25.00	0.86	0.82
25.25	0.84	0.82
25.51	0.82	0.77
25.77	0.81	0.77
26.03	0.78	0.67
26.28	0.74	0.61
26.54	0.70	0.65

colour completeness of our selected sample. This is needed, as there will be genuine PNe which lie in CMD regions outside of the colour-selection criteria because of photometric errors. The average colour completeness of our selected sample from 23.5 to 26.8 AB magnitudes was 81% and the magnitude-binned values are presented in Table A.1.

Similarly, we determined the spatial completeness by determining the recovery fraction of the simulated population within the limiting magnitude as a function of major-axis radius (see Table B.1).

Appendix B: The $z = 3.1$ Ly- α luminosity function

Gronwall et al. (2007) carried out a deep survey for $z = 3.1$ Ly- α emission-line galaxies. The LF is characterised by a Schechter-function (Schechter 1976)

$$\phi(L/L^*) d(L/L^*) \propto (L/L^*)^\alpha \exp(-L/L^*) d(L/L^*), \quad (\text{B.1})$$

Table B.1. Spatial completeness c_{spatial} for a range of major-axis radii r_{major} .

r_{major} [$^\circ$]	A [$^\circ^2$]	c_{spatial}	a_{frac}
0.08	0.0069	0.69	0.04
0.10	0.0084	0.79	0.94
0.13	0.0140	0.83	0.98
0.15	0.0160	0.88	0.98
0.19	0.0260	0.93	0.99
0.22	0.0290	0.86	0.95
0.28	0.0500	0.93	0.80
0.40	0.0790	0.88	0.44

Notes. A denotes the un-masked bin area and a_{frac} the unmasked fraction of a complete elliptical bin.

with parameters $\log L^* = 42.66 \text{ erg s}^{-1}$, $\alpha = -1.36$ and normalisation $\phi^* = 1.28 \times 10^{-3}$. The survey has a limiting magnitude of $m_{5007,\text{lim}} = 28.3$, which is somewhat brighter than the limiting magnitude of our study. We extrapolated the LF down to the depth of our survey, which is $m_{5007,\text{lim}} = 28.8$ (cf. Sect. 3.4).

The survey area of 0.244 deg^2 corresponds to a comoving volume of $1.84 \times 10^5 \text{ Mpc}$. However, as G07 state, the effective survey volume is roughly 25% smaller when taken through a non-square filter bandpass. Taking this into account, the total number of Ly- α emitters that we expect in our survey area is 310.

The clustering correlation length is $r_0 = 3.6 \text{ Mpc}$, which corresponds to $r'_0 = 7.9'$ at the distance of the Virgo cluster. We can thus expect about 20% variation in the LF due to large-scale cosmic variance (Gawiser et al. 2007; Somerville et al. 2004). Accounting for this variation, $(29.8 \pm 6.0)\%$ of the objects in the completeness-corrected sample are predicted to be Ly- α emitting background galaxies. Figure 10 shows the G07 Ly- α LF alongside with the LF of the selected PNe.